J. Fluid Mech. (2001), *vol.* 428, *pp.* 349–386. Printed in the United Kingdom

© 2001 Cambridge University Press

Entrainment and mixing in stratified shear flows

By E. J. STRANG AND H. J. S. FERNANDO

Environmental Fluid Dynamics Program, Department of Mechanical
and Aerospace Engineering, Arizona State University, Tempe, AZ 85287-6106, USA

(Received 30 June 1997 and in revised form 10 September 2000)

The results of a laboratory experiment designed to study turbulent entrainment at sheared density interfaces are described. A stratified shear layer, across which a velocity difference ΔU and buoyancy difference Δb is imposed, separates a lighter upper turbulent layer of depth D from a quiescent, deep lower layer which is either homogeneous (two-layer case) or linearly stratified with a buoyancy frequency N (linearly stratified case). In the parameter ranges investigated the flow is mainly determined by two parameters: the bulk Richardson number $Ri_B = \Delta bD/\Delta U^2$ and the frequency ratio $f_N = ND/\Delta U$.

When $Ri_B > 1.5$, there is a growing significance of buoyancy effects upon the entrainment process; it is observed that interfacial instabilities locally mix heavy and light fluid layers, and thus facilitate the less energetic mixed-layer turbulent eddies in scouring the interface and lifting partially mixed fluid. The nature of the instability is dependent on Ri_B, or a related parameter, the local gradient Richardson number $\overline{Ri}_g = \overline{N_L^2}/\overline{(\partial u/\partial z)^2}$, where N_L is the local buoyancy frequency, u is the local streamwise velocity and z is the vertical coordinate. The transition from the Kelvin–Helmholtz (K-H) instability dominated regime to a second shear instability, namely growing Hölmböe waves, occurs through a transitional regime $3.2 < Ri_B < 5.8$. The K-H activity completely subsided beyond $Ri_B \sim 5$ or $\overline{Ri}_g \sim 1$. The transition period $3.2 < Ri_B < 5$ was characterized by the presence of both K-H billows and wave-like features, interacting with each other while breaking and causing intense mixing. The flux Richardson number Ri_f or the mixing efficiency peaked during this transition period, with a maximum of $Ri_f \sim 0.4$ at $Ri_B \sim 5$ or $\overline{Ri}_g \sim 1$. The interface at $5 < Ri_B < 5.8$ was dominated by 'asymmetric' interfacial waves, which gradually transitioned to (symmetric) Hölmböe waves at $Ri_B > 5.8$.

Laser-induced fluorescence measurements of both the interfacial buoyancy flux and the entrainment rate showed a large disparity (as large as 50%) between the two-layer and the linearly stratified cases in the range $1.5 < Ri_B < 5$. In particular, the buoyancy flux (and the entrainment rate) was higher when internal waves were not permitted to propagate into the deep layer, in which case more energy was available for interfacial mixing. When the lower layer was linearly stratified, the internal waves appeared to be excited by an 'interfacial swelling' phenomenon, characterized by the recurrence of groups or packets of K-H billows, their degeneration into turbulence and subsequent mixing, interfacial thickening and scouring of the thickened interface by turbulent eddies.

Estimation of the turbulent kinetic energy (TKE) budget in the interfacial zone for the two-layer case based on the parameter α, where $\alpha = (-B + \epsilon)/P$, indicated an approximate balance ($\alpha \sim 1$) between the shear production P, buoyancy flux B and the dissipation rate ϵ, except in the range $Ri_B < 5$ where K-H driven mixing was active.

1. Introduction

The significance of studying the transport of scalars across an interface that separates an overlying turbulent shear flow from an underlying dense homogeneous or stratified layer has long been appreciated in the context of atmospheric and oceanic mixed layers and a variety of industrial situations. For instance, through the action of the surface wind stress and convection driven by surface cooling (especially at night), the upper ocean is maintained in a turbulent state. The tendency of turbulence to diffuse into the adjoining non-turbulent layer leads to the erosion of the underlying stratification of the thermocline (the 'entrainment' phenomenon), thus increasing the mixed-layer thickness. Through various mechanisms, not yet completely understood, the entrainment occurs at the turbulent/non-turbulent interface (the so-called entrainment interface) permitting the transport of hydrophysical properties such as heat, salinity and eco-system nutrients between the upper and lower layers of the oceans. The transported scalars redistribute throughout the turbulent layers and finally mix irreversibly at the molecular scales, thus substantially changing the properties of the upper layer. It is essential to understand the processes responsible for the exchange of these properties across the mixed-layer base, because it is in this region that the vertical transports in the upper ocean are controlled by buoyancy effects. On a smaller scale, this scenario is quite similar to limnological situations wherein a surface mixed layer is created when forced in a like manner at a lake surface. The entrainment occurring at lutoclines (sediment interfaces) should be contrasted with that occurring across thermo- and haloclines in that the former does not undergo irreversible mixing at the small scales (Noh & Fernando 1991; Huppert, Turner & Hallworth 1995).

Conversely, the mirror image of these situations holds true for the atmosphere over flat terrain wherein the convective turbulence generated due to surface heating causes the rise of ground-based inversions. In general, vertical shear can be present at the atmospheric inversion layers, especially in the nocturnal stable boundary layer, or at the boundaries of downward plunging cool gravity currents (katabatic winds) and rising warm air along topographic inclinations (Manins & Sawford 1979; Andrè & Lacarrère 1986). The rate of rise of an inversion or mixing across atmospheric stratified layers sensitively determines the predictions of ground pollutant concentrations in air pollution models. Moreover, in coupled oceanic–atmospheric models, the coupling is accomplished via the upper ocean and lower atmospheric mixed layers and, hence, an understanding of their properties is crucial for the accuracy of such models.

In natural flows, turbulence can be generated by a variety of mechanisms, for example mean velocity shear, breaking of surface (in oceans) or internal waves, and thermal convection due to either heating of the ground (in atmospheric flows) or cooling of the ocean surface (Turner 1973, 1986). In particular, it has been long recognized that shear is a major source of mixing in natural flows, in that it not only produces turbulence via interaction with Reynolds stresses but also can directly cause mixing at stratified interfaces by exciting Kelvin–Helmholtz (K-H) instabilities. Numerical models have attempted to incorporate shear-induced mixing by invoking constraints on the evolution of quantities such as the bulk Richardson number at the interface,

$$Ri_B = \frac{\Delta b D}{\Delta U^2}, \tag{1.1}$$

where $\Delta b = g\Delta\rho/\rho_o$ and ΔU are the buoyancy and velocity jumps across the interface, respectively, and D is the mixed-layer depth (Pollard, Rhines & Thompson 1973;

Price, Weller & Pinkel 1986). Or, conditions for shear-induced mixing are obtained by imposing certain limiting values on the local gradient Richardson number defined as

$$Ri_g = \frac{\partial b/\partial z}{(\partial u/\partial z)^2} = \frac{N_L^2}{(\partial u/\partial z)^2} \tag{1.2}$$

(Price *et al.* 1986; DeSaubies & Smith 1982; Kundu & Beardsley 1991), where b is the buoyancy, N_L is the local Brünt–Väisälä frequency, u is the streamwise velocity and z is the vertical coordinate. In another class of models, assumptions on the energetics at the interface are utilized (Mahrt & Lenschow 1976) together with an assumed form of the vertical velocity and/or density profiles above the interface. For example, slab models assume well-mixed hydrophysical and velocity fields in the mixed layer whereas Csanady (1978) suggested that the velocity profile near a sharp interface should be logarithmic (the so-called 'law of the interface').

Although a wide variety of modelling assumptions exist, many of them have not been tested using either controlled laboratory experiments or field observations. Except for a few cases (Stephenson & Fernando 1991; Sullivan & List 1993, 1994), previous shear-driven stratified mixed-layer deepening experiments have focused on delineating the entrainment law, i.e. the relationship between the entrainment coefficient $E = u_e/\Delta U = |\mathrm{d}D/\mathrm{d}t|/\Delta U$ and the governing parameters such as the bulk Richardson number Ri_B, where u_e is the entrainment velocity. E is usually written in the form

$$E = a_1 Ri_B^{-n}, \tag{1.3}$$

where a_1 and n are constants. For further details regarding the experimental study of the entrainment law, see Ellison & Turner (1959), Kato & Phillips (1969), Kantha, Phillips & Azad (1977), Deardorff & Willis (1982) and Turner (1986).

The present laboratory experimental work was motivated by this lack of detailed information on certain key issues with regard to mixing at sheared interfaces. To this end, we have attempted to use detailed hot-film anemometry, laser-Doppler velocimetry (LDV) and conductivity measurements taken in entraining stratified fluids to evaluate important velocity, time and length scales, as well as velocity, density and their gradients, and to correlate them with quantitative flow visualization studies made with laser-induced fluorescence (LIF).

The experiments were performed in an Odell–Kovasznay type recirculating water channel, with the upper mixed layer driven over a stagnant layer of either dense homogeneous or linearly stratified fluid. This flow configuration is noted to have better flow quality (Narimousa & Fernando 1987) than the conventionally used surface screen-driven annular experiments of Kato & Phillips (1969) and the like. In § 2, we introduce two non-dimensional parameters, namely Ri_B and f_N, upon which measurable properties depend. The experimental and data analysis methods used are given in § 3.

In § 4, we will show how Ri_B and a related (locally defined) average gradient Richardson number $\overline{Ri}_g$ govern various types of instabilities leading to mixing at the interface. In particular, we will show the existence of different entrainment laws for regimes governed by different interfacial instabilities. A noteworthy observation is the transition from predominantly Kelvin–Helmholtz (K-H) instabilities to symmetric Hölmböe instabilities through a transition regime at $3.2 < Ri_B < 5.8$ or $0.36 < \overline{Ri}_g < 1.3$, where the overbar denotes (suitably) averaged values. This regime is interesting, in that K-H and asymmetric wave-type instabilities coexist in $3.2 < Ri_B < 5$ and only asymmetric waves appear in $5 < Ri_B < 5.8$. Coincidentally,

using high-resolution entrainment measurements, it was found that the interfacial mixing rate peaks at $Ri_B \sim 3-4$, possibly due to the fact that, at this Ri_B, both K-H and asymmetric waves have comparable frequencies, thus resonating with each other. In support of the entrainment measurements of § 4, interfacial buoyancy flux measurements are given in § 5.

As will be discussed in § 4 and § 5, in the parameter range $1.5 < Ri_B < 5$ there is a reduction of entrainment rate when the deep layer is stratified. Internal wave radiation off the base of the mixed layer is substantial (up to 50% of the energy flux utilized for mixing) in this regime. In § 6, we will explain why this is so, and allude to field measurements of Zic & Imberger (2000) who observed a similar phenomenon in Lake Argyle. It will be shown that 'low' frequency (i.e. ~ 0.1 Hz) interfacial 'swelling' events are responsible for the excitation of these waves. Moreover, the swelling phenomenon is a key mechanism of entrainment and mixed-layer deepening in the K-H regime.

In § 7, the measured velocity profiles away from the interface will be analysed vis-à-vis the proposal of Charnock (1955) and Csanady (1978) that they can be approximated by a logarithmic law with a Richardson-number-dependent roughness. Lastly, in § 8, we will evaluate the energetics of interfacial mixing and show that the entrainment is most efficient (i.e. with a flux Richardson number $Ri_f \sim 0.4$) at the critical Richardson number of $Ri_B \simeq 5$ or $\overline{Ri}_g \simeq 1$. Furthermore, when $Ri_B > 5$, the entrainment zone can be considered to be in quasi-equilibrium to a good approximation, while at values of $Ri_B < 5$, the balance of turbulent shear production, buoyancy flux and dissipation strays due to increased significance of wave energy input to the interfacial layer and non-stationarity. The paper concludes with a summary and a discussion in § 9.

2. Theoretical preliminaries

Let us assume that the experiments are started with a given stratification, and the initial transients cause the development of a turbulent layer of depth D_o and velocity U_m, separated from the bottom linearly stratified layer of buoyancy frequency N by a density interfacial layer of small thickness δ_o ($\delta_o/D_o \to 0$) across which the buoyancy jump is Δb_o and the velocity jump is ΔU_o. This flow situation has been used in previous experiments (e.g. Narimousa, Long & Kitaigorodskii 1986), and can be assumed as the initial condition ($t = 0$) for the later development of the mixed layer according to that schematically shown in figure 1. At a time $t = t$, the mixed layer has grown to a depth D, and the density interface has a thickness δ_b, across which the buoyancy jump is Δb. The shear layer that develops above the interface has a thickness δ_s across which the velocity changes by ΔU ($\simeq U_m$). The buoyancy gradient in the turbulent layer of depth D can be considered as dynamically unimportant, although at small Ri_B an intermediate-density layer develops between the well-mixed and interfacial layers (Fernando 1986).

In this flow configuration, turbulence can be generated by several mechanisms: the pump, the interfacial region and the sidewalls. Careful design of the pump can minimize its contribution (De Silva 1991; Strang 1997). The mean shear–Reynolds stress interaction at the sidewalls and above the interface is a definite turbulence-producing mechanism, while an additional mechanism is the instabilities that may develop at the sheared interface. The velocity and length scales of turbulence produced by both of these shear layers are expected to scale with the velocity U_m (or ΔU) and the depth of the mixed layer D (as shown later). The width of the channel W can be neglected when $D/W < 2/3$, a condition satisfied in our experiments (Kantha

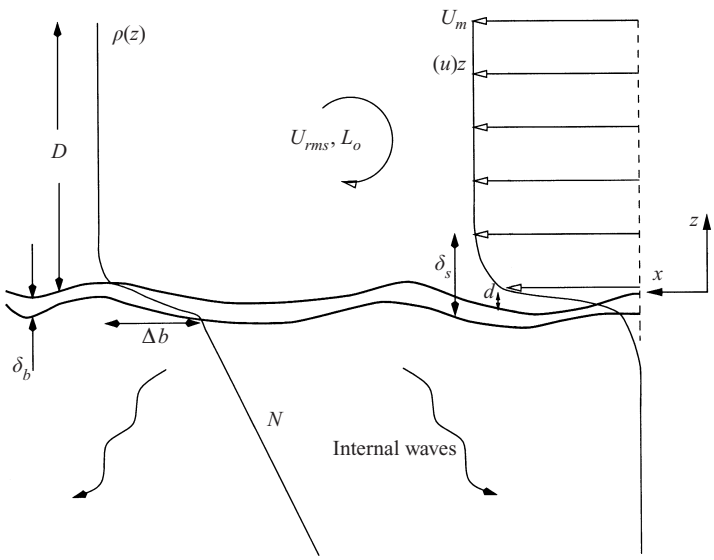

FIGURE 1. Schematic of the velocity and density field for the entrainment problem ($z = 0$ represents the mean location of the interface), where $\Delta b = g\Delta\rho/\rho_o$ is the buoyancy difference across a density interface of thickness δ_b, ΔU is the velocity difference across a shear layer of thickness δ_s whose centre is offset a distance d from the centre of the density interface. The density/velocity interface separates a turbulent mixed layer of thickness D, r.m.s. velocity scale u_{rms} and integral length scale L_o from a quiescent homogeneous layer or linearly stratified layer with buoyancy frequency N.

et al. 1977). Sidewall turbulence can interact with the interfacial shear layer and amplify shear-layer Reynolds stresses (Gartshore, Durbin & Hunt 1983) and hence the turbulent kinetic energy; but this contribution is expected to be less than 10% of the total shear stress. Consequently, the major contribution to interfacial mixing comes from the locally produced turbulence.

The governing parameters for the problem, thus, can be considered as the initial parameters at $t = 0$, i.e. Δb_o, ΔU_o and D_o, the time elapsed t, the background stratification N and the molecular parameters, the kinematic viscosity ν and the molecular diffusivity of the stratifying solute κ. Any dependent property Π at time t, therefore, becomes

$$\Pi = f_1(\Delta b_o, D_o, \Delta U_o, N, \nu, \kappa, t), \tag{2.1}$$

where $f_1, f_2, \ldots$ are functions. Successively taking Π to be the velocity difference ΔU, the depth of the mixed layer D and the buoyancy jump Δb at time t, allows Δb_o, t and ΔU_o to be eliminated from (2.1) yielding

$$\Pi = f_2(\Delta b, D, \Delta U, N, \nu, \kappa, D_o). \tag{2.2}$$

The non-dimensional form of Π can thus be written as

$$\Pi^* = f_3(Ri_B, f_N, Sc, Re, D_o/D), \tag{2.3}$$

where Ri_B is defined in (1.1), $f_N = ND/\Delta U$ is the ratio of the buoyancy frequency of the lower layer and the characteristic frequency of the mixed layer ($\Delta U/D$), $Sc = \nu/\kappa$ is the Schmidt number and $Re = \Delta UD/\nu$ is the Reynolds number. Note that $\Delta U/D$ becomes the frequency of upper-layer energy-containing eddies, in view of the fact that

$u_{rms} \simeq 0.12\Delta U$ and $L_{11} \simeq 0.18D$, where u_{rms} and L_{11} are the root-mean-square (r.m.s.) of velocity fluctuations and the longitudinal integral scale of turbulence, respectively (Stephenson & Fernando 1991; Strang 1997). Thus, the frequency scale of turbulence is $u_{rms}/L_{11} \simeq 0.66\Delta U/D$. The function Π^* is expected to be independent of D_o/D when D_o/D is small, a limit approximately satisfied in our experiments. Thus, (2.3) becomes

$$\Pi^* = f_3(Ri_B, f_N, Sc, Re). \tag{2.4}$$

Also note that there is an exact relationship in the form

$$(D + \tfrac{1}{2}\delta_b)\Delta b - \tfrac{1}{2}N^2(D + \delta_b)^2 = D_o\Delta b_o - N^2 D_o/2, \tag{2.5}$$

which follows from the integration of the buoyancy conservation equation across the upper mixed and interfacial layers.

When Re is large (in the present experiments, $Re \sim 10^4$), Π^* becomes independent of Re (Reynolds number similarity). Likewise, at large Péclet numbers $Pe = \Delta UD/\kappa$ (equivalent to $ReSc$), Π^* can be considered as independent of Sc. This follows from the fact that the time required to erase scalar gradients (mix) at the molecular diffusive scales is much less than that required to break down (stir) the large-scale inhomogeneities of scalar introduced in the mixed layer via entrainment. The latter time scale is approximately an eddy turnover time τ_E $(= L_{11}/u_{rms})$ whereas the former is proportional to $\tau_E Re^{-1/2}\ln(Sc)$; the rate limiting step has a time scale of τ_E irrespective of molecular effects (Fernando & Hunt 1996). Hence, in the finite- Sc and large- Re limit, the entrainment coefficient E becomes

$$E = E(Ri_B, f_N). \tag{2.6}$$

3. Experimental approach

Experiments were performed in a closed-loop water facility with a dual stack, counter-rotating disk pump assembly designed after that of Odell & Kovasznay (1971). A schematic of the apparatus is shown in figure 2. The disk pump imparts mean momentum to the upper layer and, hence, generates a velocity difference ΔU between the two layers. Stratification was established using salt and an aqueous solution of ethanol (< 10% by volume). Ethanol was introduced to create an optically homogeneous medium, enabling the use of optical measurement techniques. The techniques used for stratification are the same as those described in Stephenson & Fernando (1991) for the two-layer case and Perera, Fernando & Boyer (1994) for the linearly stratified case; also see Hannoun & List (1988). Measurements were accomplished using a custom built two-point, single-component laser-Doppler velocimeter (LDV), laser-induced fluorescence (LIF), micro-sensor conductivity probes, an acoustic Doppler velocimeter (ADV) and a two component X-type hot film. The parameter range of the experiments included $0.8 < Ri_B < 30.0$ and $0 < f_N < 5$ (corresponding to $5.0 < \Delta U$ (cm s^{-1}) < 15.0, $0 < N$ (rad s^{-1}) < 1.25, $15.0 < D$ (cm) < 28.0, and $2.0 < \Delta b$ (cm s^{-2}) < 75.0. The following subsections address the measurement and signal processing approach taken to determine the local gradient Richardson number, interfacial buoyancy flux and the turbulent kinetic energy budget.

3.1. *Gradient Richardson number* $\overline{Ri}_g$

Streamwise velocity and density measurements were taken simultaneously using a two-point single-component laser-Doppler velocimeter and two-point (2×4-electrode) micro-scale conductivity probe, respectively (refer to De Silva 1991 and De Silva *et al.*

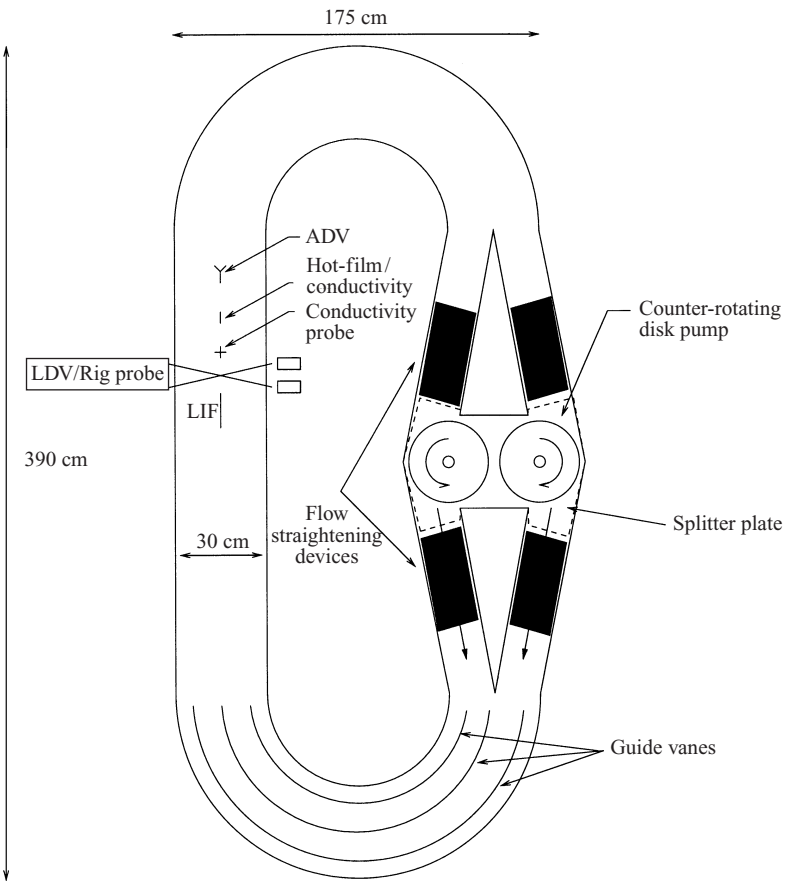

FIGURE 2. Schematic of closed-loop Odell–Kovasznay (recirculating) water facility.

1999 for details regarding the design of the components, which were custom built collaboratively with Dr Michael Head of Precision Measurement Inc.). This unique piece of hardware features the measurement of the local velocity shear $\partial u/\partial z$ to a resolution of 2.5 mm and the local density gradient $\partial \rho/\partial z$ to a resolution of 2.3 mm. Correlated measurements allow the evaluation of the instantaneous local gradient Richardson number (1.2). Measurements of Ri_g were obtained by locating the probe below the velocity and buoyancy interfacial layers and recording continuous time realizations as the interfacial region passed the probe. In so doing, a vertical distribution of Ri_g could be obtained. Time realizations were taken at 32 s intervals (separated by 10 s) with a sampling frequency of 128 Hz. This sampling time was large to resolve interfacial integral scales (the sampling frequency and time were selected to achieve sufficient frequency resolution while extracting enough samples to capture integral-scale effects and acquire 2^N sample points for FFT). The scales used for time averaging are addressed in § 3.4.

Since the density and velocity gradients in (1.2) were evaluated by discrete methods, it was possible, although infrequent, that the local instantaneous Ri_g might be nearly singular. This problem was circumvented by incorporating a running average (over a time interval of 0.04 s, 0.1% of the signal). Thereafter, time averages (over scales defined in § 3.4) were employed for the density and velocity gradients individually to

determine the average gradient Richardson number defined as

$$\overline{Ri}_g = \frac{\overline{N_L^2}}{\overline{\partial u/\partial z}^2}, \tag{3.1}$$

where the overbar denotes the respective time averages.

3.2. *Interfacial buoyancy flux*

Laser-induced fluorescence (LIF) was employed to perform detailed flow visualization, in addition to obtaining quantitative concentration measurements. An argon-ion laser and a laser beam parallel scanner (LBPS; De Silva, Montenegro & Fernando 1990) was used to produce an 8 cm wide and 0.9 mm thick laser sheet (with a nearly uniform distribution of intensity since the laser beam is scanned horizontally) in order to illuminate Rhodamine 6G dye. A 60 Hz CCD video camera with a high-pass filter and SVHS video system recorded two-dimensional time-varying fluorescent intensities. As this technique has become standard, we will not provide details here, but refer the reader to Papantoniou & List (1989) or Strang (1997) for further details.

The centre of the interface was determined by locating the isopycnal which, on average (in the streamwise direction), coincided with the maximum density gradient (zero second derivative). The spatially averaged (in the streamwise direction across the test section) location of the centre of the interface was used to determine the entrainment velocity.

When employing LIF, approximately 500 density profiles (pixel columns) equally spaced in the streamwise direction can be extracted at a given instant in time. Successive image extraction can lead to approximately 500 time traces of $b'w'$, from which a single time trace can be determined from their spatial average. Buoyancy fluctuations b' for a given spatial location are defined as $(b-\bar{b})$, where $\bar{b}$ is determined from the average (or when appropriate, a piecewise average) of the time trace. Fluctuations of the vertical interfacial velocity are determined using the displacement of the interface centre. This is represented by

$$w' \simeq \frac{\partial \eta}{\partial t} + \bar{u}\frac{\partial \eta}{\partial x}, \tag{3.2}$$

where $\eta = \eta(x,t)$, $\bar{u}$ is the local mean streamwise velocity, and no displacement of the mean location of the interface centre is assumed. It was determined that the latter term of (3.2) has only a small effect on the outcome of the measurement of $\overline{b'w'}$. The spatial average of the concurrent measurements of b' and w' determines the instantaneous averaged interfacial buoyancy flux. As discussed below, the buoyancy flux was also measured point-wise using another technique.

3.3. *TKE: shear production, buoyancy flux and dissipation*

An instrument system consisting of a two-component hot-film (X-type) and a conductivity probe was developed to measure the dissipation, buoyancy flux and shear production. Time traces of streamwise and vertical velocity and density were acquired at time intervals of 32 s at a sampling frequency of 512 Hz. Due to the temporal length of the acquisitions, piecewise averages could be applied to accommodate the local assumption of a quasi-stationary process (§ 3.4 addresses the scales for time averaging).

As described in Kit, Strang & Fernando (1997) and Strang (1997), the rate of dissipation of TKE just above the interface was calculated under the assumption of local isotropy and Taylor's frozen turbulence hypothesis. The dissipation ϵ was

estimated using either the streamwise gradient of the streamwise velocity or the streamwise gradient of the vertical velocity. Typically, the normalized skewness of the former fell in the range −0.035 to −0.058. However, at times, due to the contamination of the streamwise velocity at the high end of the frequency spectrum by probe noise, the latter derivative was used. Kit *et al.* (1997) used the condition proposed by Gargett, Osborn & Nasmyth (1984) to check the isotropy of dissipative eddies; they suggest $I = (\epsilon/\nu N^2)^{3/4} > 200$ as the criterion for the local isotropy at dissipative scales of stratified turbulence. It was found that $I \simeq 300$–500 for $Ri_B < 5$ and $I \simeq 1000$ for $Ri_B > 5$ in the upper interfacial zone (generally outside $|z/\delta_b| > 1$).

The accuracy of the measurements of shear production is dependent on that of the vertical mean velocity profile. The mean profile was evaluated using the hot-film anemometer, and it was found that representing the data through the shear layer with a hyperbolic tangent fit was an excellent approximation for the mean velocity. The mean shear could then be determined analytically within the error of the measurements and the respective fit.

As in Kit *et al.* (1997), the systematic calibration errors for the hot-film measurements were ±0.5% and the total cumulative errors of measurements were ±15% for ϵ, ±18% for shear production and ±5% for the buoyancy flux.

3.4. *Scales for time averaging*

Due to the non-stationary nature of the problem, a detailed discussion of the averaging time scales is warranted. In particular, it is essential to consider the averaging time scale vis-à-vis that of mixed-layer deepening (i.e. the time scale over which macroscopic flow properties vary significantly). On a time scale sufficiently smaller than the deepening time scale $\tau_D \sim D(\mathrm{d}D/\mathrm{d}t)^{-1}$, a time trace of velocity and density can be assumed quasi-stationary. Furthermore, as discussed earlier, the sampling interval must be chosen sufficiently long to resolve the (integral) time scale associated with energy-containing eddies τ_L in the mixed layer $\tau_L = L_{11}/\Delta U = 0.18D/\Delta U$ or the time variability in the interface due to advection of instabilities of wavelength λ, $\tau_L = \lambda/\Delta U$, as appropriate. Therefore, as a general rule within the practical limitations of the experiment, the sampling time scale t_{samp} was chosen to satisfy $\tau_L < t_{samp} \ll \tau_D$.

As discussed earlier, the time scale of mixed-layer evolution, and hence the averaging time, is dependent on Ri_B. This will be discussed in greater detail in §4 where measurements of the entrainment rate are presented. In order to satisfy the upper and lower limits on the sampling time, time averages were defined to be 5% of the mixed-layer deepening time scale, i.e. $t_{samp} \leqslant 5\%\tau_D = 0.05D(\mathrm{d}D/\mathrm{d}t)^{-1} = 0.05D/E(Ri_B)\Delta U$. Choosing the averaging time scale to be larger than the above criterion tended to bias the results, with the second-order correlations tending to increase due to the more apparent non-stationarity of the system. Conversely, selecting an averaging time scale substantially smaller than this criterion led to second-order correlations that tended to be erratic with decreasing the averaging time scale. The above criterion was further verified by inspection of the Fourier spectrum of the fluctuation signal. Note that in addition to satisfying the upper limit, t_{samp} remains substantially larger than the integral time scale, for example, for the mixed layer measurements. Since $E < 0.03$, for all Ri_B (§4.3), the sampling time (per the criterion presented) becomes $t_{samp} \sim 5D/3\Delta U$ or $t_{samp} \geqslant 10\tau_L$ for all measurements.

Based on the above criterion, at large Ri_B ($Ri_B > 10$), the interfacial movement is so slow that it is possible to profile the interface and base of the mixed layer in steps of $\leqslant$ 2 mm. For each measurement point in the flow, multiple readings ($\geqslant 2$) using an averaging time scale $\tau \geqslant 32$ s can be taken in order to accommodate an

additional ensemble average. At lower Ri_B ($4 < Ri_B < 10$), it is possible to determine a distribution of velocity and density across the interface and base of the mixed layer with a resolution $\leqslant 6$ mm using an averaging time scale of 16 to 32 s. For $Ri_B < 4$, a time record of 32 s in length appears non-stationary by inspection. For $2 < Ri_B < 4$, only a few points can be obtained across the mixed-layer base using an averaging time scale of 4 to 16 s. And lastly, it was necessary to use a running average (0.5 to 4 s in length) to determine the fluctuating quantities when $Ri_B < 2$.

Further technical details of the gradient Richardson number probe, the calibration and data handling of the LIF procedure, the calibration of the hot-film probe, the refractive index matching for the LIF, and the pre- and post-processing of data including the design of the hardware and software, quality of signals, removal of bias errors and error analysis are given in Strang (1997). That report also contains measurements and discussions of flow quality in the channel, performance of the Odell–Kovasznay pump and isolation of turbulence generated at the pump, and a detailed discussion of the space–time scales used in averaging.

4. Observations and measurements of entrainment

4.1. *Entrainment mechanisms*

A schematic of typical density and velocity profiles observed during experiments, excluding transient features, is shown in figure 1. As stated in § 3, the velocity profile near the interface can be approximated to a hyperbolic tangent profile with a thickness δ_s, which embodies a thinner density interface of thickness δ_b. Furthermore, the centre of the density interface is offset from that of the shear layer by a length scale d. All three scales defining the stratified shear layer depicted in figure 1, i.e. δ_s, δ_b and d, are mainly determined by Ri_B and f_N, as will be discussed later. At large $Ri_B (> 1)$, eddies in the upper turbulent layer (with inertial forces $\sim \Delta U^2/D$) are too feeble to penetrate into the interface and encroach non-turbulent fluid against their buoyancy forces ($\sim \Delta b$), thus shutting off the conventional entrainment mechanism (namely, eddy engulfment) occurring in non-stratified fluids. Under these conditions, the entrainment takes place by diluting interfacial fluid locally via mixing induced by interfacial instabilities to an extent that permits the lifting and transporting of partially mixed fluid into the turbulent layer (Fernando 1991). Therefore, interfacial instabilities and their breakdown in stratified shear layers play a key role in mixed-layer deepening, as will be further discussed below.

Stability studies of stratified shear layers date back to the work of Taylor (1931) and Goldstein (1931) on continuously stratified unbounded parallel shear flows. Miles (1961), considering monotonic velocity and density profiles, proved that a necessary condition for instability is that the gradient Richardson number $Ri_g = N_L^2/(\partial u/\partial z)^2$ should be less than 0.25 somewhere in the flow. Howard (1961) immediately generalized this result and removed the restriction on monotonicity. Thorpe (1968), through laboratory experiments, identified solutions to the Taylor–Goldstein (1931) equations and illustrated that the first mode appearing when $Ri_g < 0.25$ is the Kelvin–Helmholtz (K-H) instability. Numerical calculations of Hazel (1972), with hyperbolic tangent profiles for velocity and density of equal (interfacial) thicknesses, corroborated Thorpe's result and showed that the wavelength λ of the fastest growing disturbances is only weakly dependent on Ri_g with $\lambda \sim 7\delta_s$; see Kundu & Beardsley (1991). The presence of boundaries makes long waves more susceptible to instabilities (Hazel 1972), but the boundary effects are negligible when the total height of the water column H is large

compared to the shear layer thickness, $H > 5\delta_s$ (Haigh & Lawrence 1999), which is a condition satisfied in our experiments.

As noted by Hölmböe (1962) and Hazel (1972), when $\delta_s > \delta_b$, as in the present experiments, the flow phenomena in the interface are complex with the type of instabilities sensitively dependent on the details of the velocity and density profiles. Since the experimental profiles in general are dependent on Ri_B and f_N, the nature of the instabilities ought to be governed by these two parameters, a deduction that will be shown to be consistent with our observations. Hölmböe (1962) showed that, in the limits $\delta_b/\delta_s \to 0$, $N = 0$ and $e = d/\delta_s = 0$, there exists an additional instability, the Hölmböe instability. Thence, the parameter determining the flow was found to be the shear-layer Richardson number $Ri_s = \Delta b\delta_s/\Delta U^2$ (which is directly related to Ri_B as $Ri_s \simeq 0.1Ri_B$, given $\delta_s = 0.11D$; § 2). The flow was linearly unstable to two types of instabilities, with K-H instabilities possible at $Ri_s < 0.071$ and Hölmböe instabilities appearing at all $Ri_s > 0$. When $Ri_s < 0.046$, the growth rate of the fastest K-H mode was larger than the Hölmböe mode and hence K-H instability dominates the flow. When $Ri_s > 0.071$, only the Hölmböe mode is possible. In contrast to the $\delta_s = \delta_b$ case described before, the wavelengths of the fastest growing modes here are sensitive to Ri_s. In terms of identifiable traits, the K-H instabilities are characterized by a zero phase speed relative to the centre of the interface and a distinctive rolling up of the interface to produce a series of billows (Klaassen & Peltier 1989). Conversely, the Hölmböe waves are signified by the superposition of two unstable modes of equal growth rates and equal but opposite phase speeds with energy in one mode concentrated above the centre of the interface and in the other concentrated below the centre of the interface.

The case of $e \neq 0$ and $\delta_b/\delta_s \to 0$, which is more relevant to the present experiments, has been studied by Lawrence, Browand & Redekopp (1991) and Haigh & Lawrence (1999) who also identified additional modes of instability. The asymmetry introduced by $d \neq 0$ leads to an asymmetry of Hölmböe instabilities, in that usually symmetric Hölmböe waves now become *one sided*, with an amplifying instability wave protruding into one of the layers and an additional wave in the adjacent layer fading away (also see Koop & Browand 1979). Henceforth, these waves will be referred to as asymmetric waves. No *pure* K-H or symmetric Hölmböe waves were predicted for the $e \neq 0$ case. The instability waves appearing for this case were characterized by the phase speed relation $c_r^R + c_r^L = -e$, where c_r^R is the phase speed of the right moving wave normalized by $\Delta U/2$ and vice versa. This implies that both waves move at equal speeds but in opposite directions relative to the velocity of the density interface.

Although the profiles of our experiments are not strictly identical to those used for stability analyses described above and the presence of turbulence in the upper layer leads to finite-amplitude forcing, it was possible to place our interfacial observations in the context of linear stability predictions. These comparisons, however, should be construed as qualitative and, therefore, not all quantitative predictions of the linear stability theory are borne out by our measurements. Figure 3(*a–h*) shows false colour images (image width $\simeq 6.5$ cm) representing spatial distributions of the concentration field and the morphology of the interface (there is a one-to-one relationship between the vertical and horizontal scales of the image). The threshold level representative of the background concentration, however, has been subtracted and the resultant image is then stretched over the intensity range (0 to 255). This was performed on all images in order to produce an improved contrast of interfacial disturbances, in particular K-H billows which develop at the upper edge of the interfacial layer.

Figure 3(*a*, *b*) shows interfacial instability for $Ri_B = 1.8$ ($\overline{Ri}_g = 0.12$, $Ri_s = 0.20$,

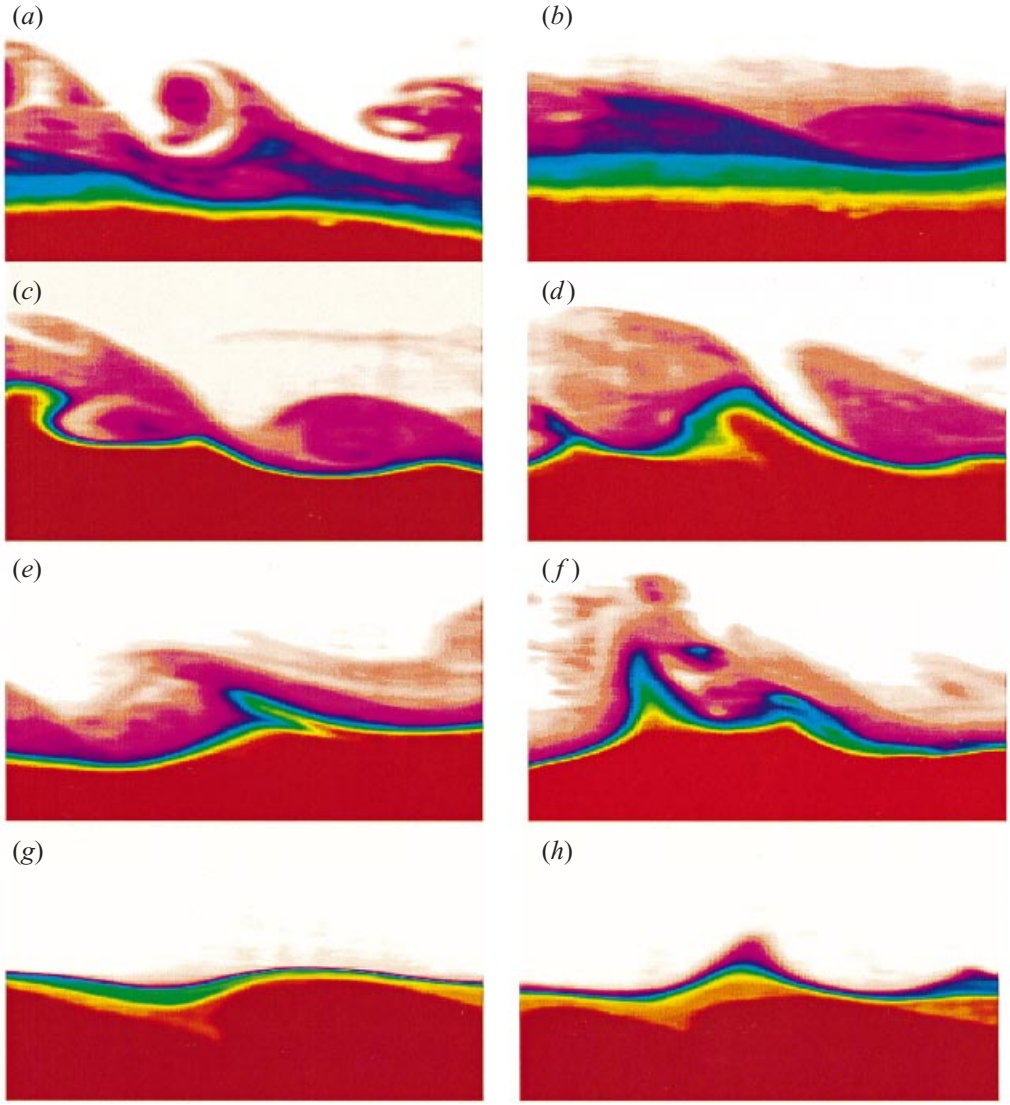

FIGURE 3. Entrainment mechanisms: (*a*) K-H billows, $Ri_B = 1.8$ and $\overline{Ri}_g = 0.12$; (*b*) K-H billows, $Ri_B = 3.2$ and $\overline{Ri}_g = 0.36$; (*c*) convoluted interface with mixed K-H billowing and wave breaking activity, $Ri_B = 4.5$ and $\overline{Ri}_g = 0.83$; (*d*) wave distortion by shear, $Ri_B = 5.5$ and $\overline{Ri}_g = 1.21$; (*e*) shortly after (*d*) whence the wave crest continues to distort, $Ri_B = 5.5$ and $\overline{Ri}_g = 1.21$; (*f*) wave breaking event, $Ri_B = 5.8$ and $\overline{Ri}_g = 1.78$; (*g*) symmetric Hölmböe waves, $Ri_B = 9.2$ and $\overline{Ri}_g = 2.82$; (*h*) Hölmböe waves, $Ri_B = 9.2$ and $\overline{Ri}_g = 2.82$.

$e \simeq 0.2$) and $Ri_B = 3.2$ ($\overline{Ri}_g = 0.36$, $Ri_s = 0.35$, $e \simeq 0.11$). The overturning structure as well as their approximately zero phase speed relative to the centre of the shear layer suggest their similarity to K-H instabilities. This is further corroborated by the measurements of the Thorpe length scales $L_{T\,rms}$ (Thorpe 1977) within the billows, in that, along a line passing through the centre of the billows, the ratio of $L_{T\,rms}$ to the maximum Thorpe scale $L_{T\,max}$ is 0.567. This agrees well with the measurements of De Silva *et al.* (1996) made in tilting tank experiments who found $L_{T\,rms}/L_{T\,max} = 0.576$

at a comparable Ri_s. The above length-scale ratio and qualitative 'roll-up' features were used to recognize K-H instabilities in all of the cases described throughout this paper.

As mentioned, linear stability analysis of Haigh & Lawrence (1999) predicts neither pure K-H nor Hölmböe instabilities for the Ri_s and e values noted, though, in certain parameter ranges, our observations show instabilities closely resembling one or the other. The differences can be attributed to the finite-amplitude nature of forcing and the sensitivity of instabilities to the details of velocity profiles. According to Haigh & Lawrence (1999), the fastest growing instabilities for $Ri_s = 0.20$ and $e = 0$ with $\delta_b/\delta_s \to 0$ have a wavelength of about $4.2\delta_s$ or 6.3 cm. When $e \simeq 0.2$, several other prominent modes can appear with wavenumbers both larger and smaller than 6.3 cm, one of which is 3.8 cm. The observed average wavelength 3.3 cm is close to this prediction and the instability appears to be of K-H type. Note that the observed instability wavelength for this case is much smaller than $7\delta_s = 10.5$ cm predicted by linear stability calculations for continuously stratified cases and 11.5 cm as predicted for the hyperbolic tangent profiles with $\delta_s/\delta_b = 2$ and $e = 0$ (Hazel 1972). The observations for $Ri_B = 3.2$ were also generally the same. A noteworthy observation from figure 3(a, b) is that the K-H billows appear at the top of the interface, in the region where the local Ri_g is smallest (which agrees with the calculations of Hazel 1972). The lower side of the interface is approximately flat while on the upper edge K-H billows grow and degenerate into turbulence. In all, though the stability theory suggest neither pure K-H nor Hölmböe instabilities but something in between, in the range $1.5 < Ri_B < 3.2$ of the current experiments, instabilities similar to K-H billows could be observed. Note that the Ri_B limits stated throughout the paper are based on multiple observations. They are subjected to $\pm 10\%$ uncertainty.

The K-H billows in our experiments were found to degenerate into turbulence rapidly, causing intense local stirring. Owing to the limitations of the flow diagnostic methods used, the details of the turbulence generation could not be identified, but sequences of LIF images show how small-scale features first appear surrounding the eye of the billow, in the convectively unstable region. This points to the possibility of secondary instabilities such as longitudinal roll vortices (Klaassen & Peltier 1989) that burst into turbulence via twist wave dynamics (Fritts, Arendt & Andreassen 1998) or jet-type 'near-core' instabilities surrounding the centre of billows (Staquet 1995). Although secondary instabilities may also arise in the braid region of K-H billows, they were not evident in the present experiments; these would have included the secondary K-H instability (Staquet 1995) and the braid instability (Klaassen & Peltier 1989). Other sub-harmonic instabilities such as vortex amalgamation and vortex deformation and vortex draining by the neighbours were also not prominent.

Beyond $Ri_B \sim 3.2$, the nature of the interface drastically changed, in that the relatively flat interface below the K-H billows transformed into a highly distorted surface bearing wave-like disturbances (figure 3c–f). Billows of K-H nature coexisted with these wave-like disturbances, but with decreasing frequency with increasing Ri_B. The K-H and wave-like features violently interacted with each other, causing strong turbulent mixing. It appears that K-H billows and these disturbances have similar frequencies, causing resonance between the two types of disturbances.† Because of their rapid evolution, systematic eduction of quantitative information pertinent to the wave disturbances was difficult, but their qualitative behaviour was similar to that of one-sided asymmetric waves described by Lawrence *et al.* (1991) and Haigh & Lawrence

† We are grateful to Professor J. C. R. Hunt for pointing out this possibility.

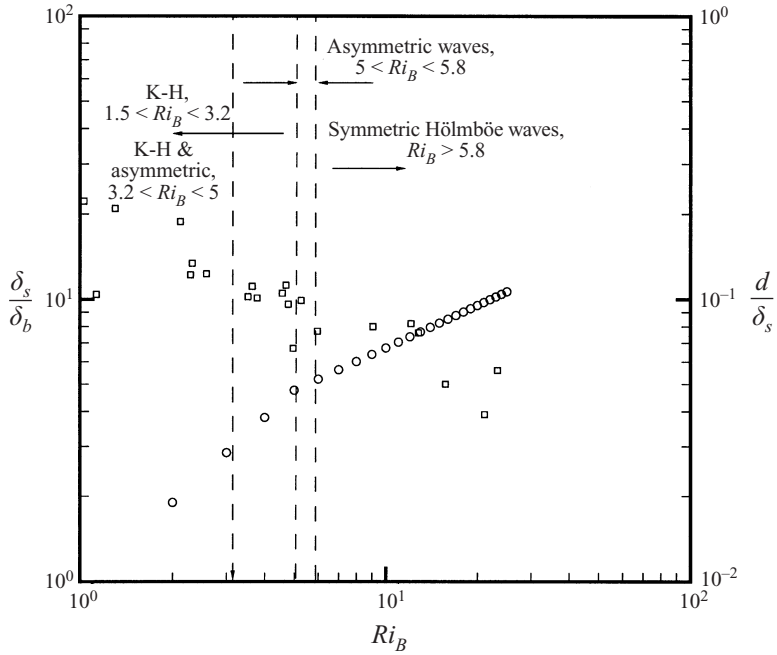

FIGURE 4. Ratio of velocity to density length scales δ_s/δ_b (○) and the normalized interfacial displacement d/δ_s (□) as a function of Ri_B. The regions of demarcation between K-H and symmetric Hölmböe instabilities are indicated.

(1999). With increasing Ri_B, the K-H activity subsided and was virtually non-existent at $Ri_B > 5$. Thereafter, the interface was dominated by asymmetric waves, signifying the asymmetry of interfacial profiles. Evidently, $3.2 < Ri_B < 5$ represents a regime wherein the flow transitions from a predominantly K-H regime ($1.5 < Ri_B < 3.2$) to one dominated by asymmetric waves. The dominant feature in $5 < Ri_B < 5.8$ was the intermittently breaking asymmetric waves.

$Ri_B > 5.8$ is characterized by symmetric Hölmböe instabilities. At $Ri_B \simeq 5.8$, the displacement d between the density and velocity profiles (figure 4) is sufficiently small to bestow some symmetry on the interface, thus facilitating 'two-sided' Hölmböe waves with cusps on opposite sides moving in opposite directions (figures 3(g, h)). The identity of these Hölmböe waves was established by measuring the phase speeds of the left c_r^L and right c_r^R moving waves with respect to the velocity of the density interface, which ought to be the same. For example, for the waves shown in figure 3(g, h), $c_r^L = 3.0\,\mathrm{cm\,s^{-1}}$ and $c_r^R = 3.1\,\mathrm{cm\,s^{-1}}$. The transition to the Hölmböe regime was marked by a reduction of d/δ_s, a change of the behaviour of δ_s/δ_b (figure 4) and a drop in mixing activity leading to a substantial drop in the entrainment rate (§ 4.3).

4.2. *The gradient Richardson number*

The above discussion was presented in terms of the bulk Richardson number of the flow, but it is common in field studies (e.g. Moum, Caldwell & Paulson 1989; Kundu & Beardsley 1991) to express the stability of the flow in terms of the local gradient Richardson number Ri_g measured at a suitable resolution as the interfacial instabilities are thought to be governed by Ri_g (which may not necessarily be the case, as the above discussion of stability theory indicates). As discussed in § 3.1, because of the variability of Ri_g, it is customary to use the averaged gradient Richardson

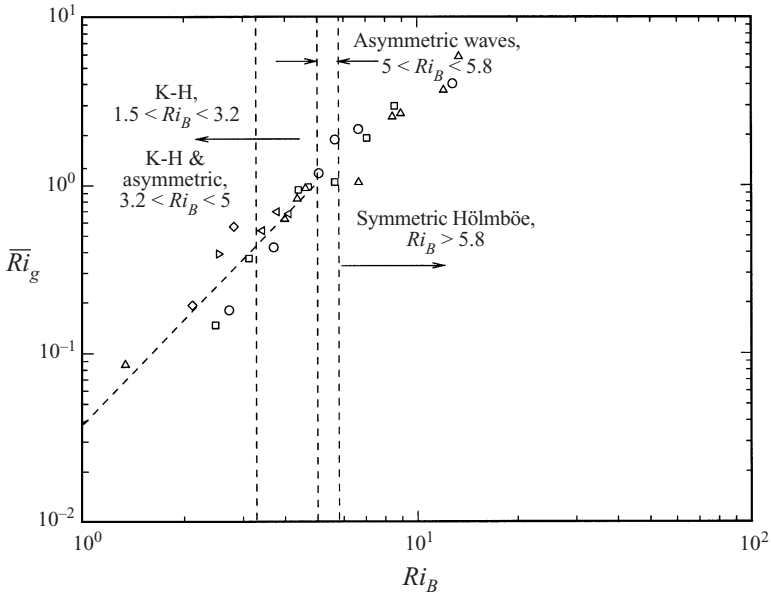

FIGURE 5. Relationship between average minimum gradient Richardson number $\overline{Ri}_g$ and Ri_B (different symbols indicate different experiments). Note the change of the relationship at $Ri_B \sim 5$ where K-H instabilities disappear.

number $\overline{Ri}_g$, namely

$$\overline{Ri}_g = f_4(Ri_B, f_N). \tag{4.1}$$

Moreover, De Silva *et al.* (1999) have shown that $\overline{Ri}_g$ is independent of the measurement resolution Δz_m provided that $\Delta z_m < L_R$, where $L_R = (\epsilon/N^3)^{1/2}$ is the Ozmidov length scale. Since $\Delta z_m \simeq 2.3$ mm and typical values for L_R in the upper interfacial zone are $0.4 < L_R < 3.2$ cm, Δz_m is not included in (4.1). Figure 5 presents $\overline{Ri}_g$ versus Ri_B. The slope of $\overline{Ri}_g$ versus Ri_B for $Ri_B < 5$ was determined (using a least squares fit) to be 2.05 ± 0.20, indicating $\overline{Ri}_g \propto Ri_B^2$, irrespective of f_N. This is consistent with the definition of a 'bulk' gradient Richardson number $Ri_g^b = (\Delta b/\delta_b)/(\Delta U/\delta_s)^2$,

$$Ri_g^b = Ri_s \frac{\delta_s}{\delta_b}. \tag{4.2}$$

Since $\delta_s/D \sim$ constant and $\delta_b/D \sim Ri_B^{-1}$ for $Ri_B < 5$, $\overline{Ri}_g^b \propto Ri_B^2$ can be expected. Based on figure 5, various entrainment regimes identified above can be recast in terms of $\overline{Ri}_g$. When $\overline{Ri}_g < 0.36$, the entrainment interface is dominated by K-H billows, followed by a regime $0.36 < \overline{Ri}_g < 1$ where a resonant combination of K-H billows and asymmetric waves occurs, and then asymmetric waves prevail in $1 < \overline{Ri}_g < 1.3$ and lastly leading to a regime $\overline{Ri}_g > 1.3$ where Hölmböe waves are prevalent. The critical $\overline{Ri}_g$ where the K-H instabilities disappear is $\overline{Ri}_{gc} \simeq 1$.

The measurement of mixing efficiency (see § 8) clearly shows a maximum when $Ri_B \sim 4.7$–5.3 or so, or when $\overline{Ri}_{gc} < 0.9$–1.1, which is approximately coincident with a substantial decline of the entrainment velocity by at least one order of magnitude above $Ri_B > 5.8$ or $\overline{Ri}_g > 1.3$. In passing, it should be noted that the above $\overline{Ri}_{gc}$ is greater than the cannonical $Ri_c \simeq 1/4$ occurence, which is necessary somewhere in the flow for linear instability based on Miles–Howard (1961) theory. This is expected

because the time scale over which the mean gradient Richardson number is averaged is long relative to the time scale associated with the growth of K-H waves and, therefore, it does not necessarily represent the local gradient Richardson number at the interface prior to the growth of K-H instability. In fact, the averaging time scale includes a substantial fraction of the interfacial swelling period. In other words, the averaging time scale includes periods of large Ri_g where K-H billows collapse to mix and thicken the interfacial layer as well as periods of negative Ri_g where overturning of the interfacial layer occurs. Moreover, the broadband and finite-amplitude nature of excitation and the nature of velocity and density profiles as described in § 4.1 could also be responsible. It is also interesting to note that the stability estimates based on energy considerations (Richardson 1920; Taylor 1931) and Liapunov analysis (Abarbanel *et al.* 1986), which accommodate finite-amplitude perturbations, imply that $Ri_{gc} \simeq 1$ (also see Miles 1986), in consonance with the present observations. The original eddy transport model of Richardson (1920) also predicts $Ri_{gc} \simeq 1$.

What are the implications of the measured Ri_{gc} in the context of oceanic flows? Thompson's (1984) analysis of oceanic Richardson number data of DeSaubies & Smith (1982) indicates that the probability of shear-controlled mixing in oceans becomes negligible when $Ri_g > 1.33$. This observation is consistent with the entrainment data presented in § 4.4, which show a substantial decrease of the entrainment rate beyond $Ri_B > 5$–6 or $\overline{Ri}_g > 1.3$. This implies that for practical purposes, the cut-off of entrainment can be considered to occur above $\overline{Ri}_g \simeq 0.7$–1.3 or $Ri_B \simeq 4.3$–5.8.

The mixed-layer forecasting model of Price *et al.* (1986), currently used for US Naval applications, employs, among other constraints, critical values of $Ri_{gc} = 0.25$ and $Ri_{Bc} = 0.65$ above which the entrainment is negligible. Given that Ri_g is a function of Ri_B, one of these constraints appears to be redundant, if mixing is shear dominated. This assertion has been echoed by numerous practitioners who have noted the insensitivity of predictions to the Ri_B criterion employed in the Price *et al.* (1986) model (Professor E. D'Asaro, personal communication).

During the past decade or so, many oceanic and atmospheric observations of Ri_g have been reported, and some results are the following:

(*a*) Observations in the main thermocline near Bermuda by Eriksen (1978) show that, under calm oceanic conditions, Ri_g assumes large values. As effective mixing events intermittently appear, signified by the generation of inversions in the density profiles, Ri_g drops to values below unity, the critical value specifically tending to be in the range $0.25 < Ri_g < 1$.

(*b*) In active oceanic turbulent shear zones (high TKE dissipation and low stratification) such as equatorial undercurrents, $\overline{Ri}_g$ tends to remain below about unity, while in substantially stratified shear zones (low dissipation and high stratification) $\overline{Ri}_g \sim 1$ (Moum *et al.* 1989; see their the cruise-averaged vertical profiles of Ri_g in figure 6). A further discussion in this context is given in Strang & Fernando (2000).

(*c*) In recent field experiments performed in the valley basin of Phoenix, Arizona, measurements of the local gradient Richardson number and particulate concentration across the low-level atmospheric inversion layer indicated high ground-level particulate concentrations arising from significant fluxes across the interfacial layer occurs when $\overline{Ri}_g \leqslant 1$; see Pardyjak *et al.* (1999).

In summary, the above discussion alludes to an interesting aspect of natural flows. That is, in calm pycnoclines with little shear, Ri_g is large but the stratified region intermittently becomes unstable and forms patchy turbulence, possibly because of a local drop of Ri_g below the critical value (due to the enhanced local shear resulting from the superposition of internal waves); Fernando & Hunt (1997). When the region

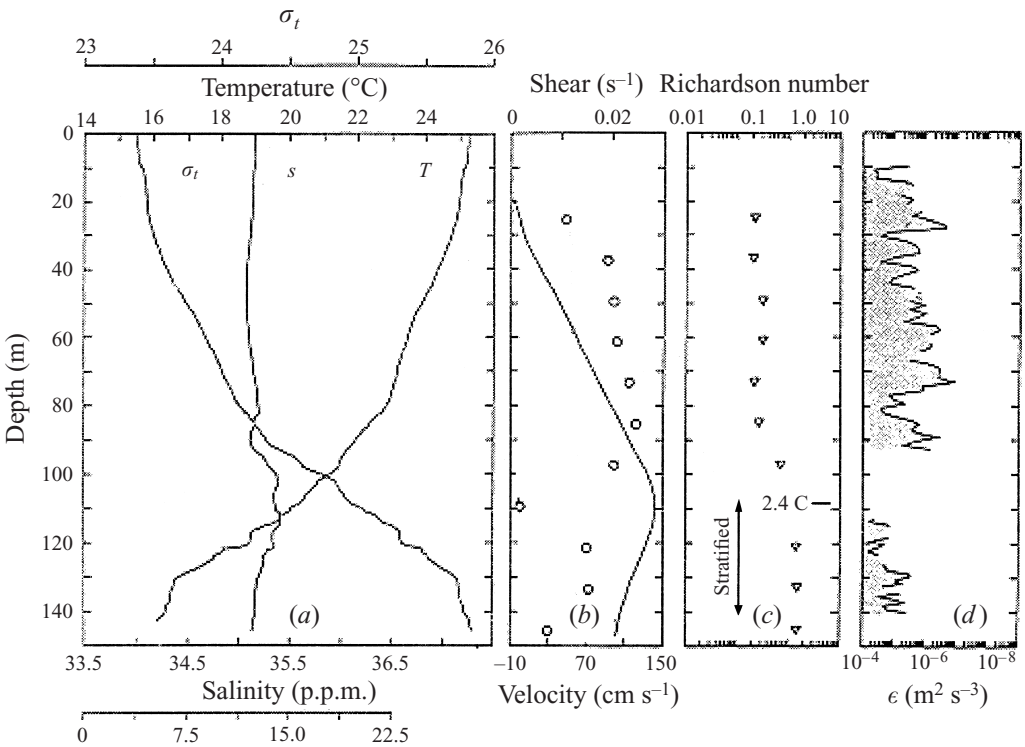

FIGURE 6. Typical daytime profile of vertical structure in a strong equatorial undercurrent: (*a*) temperature, salinity and σ_t; (*b*) closest hourly average of east-west currents as measured by the Acoustic Doppler Current Profiler, and shear magnitude (circles); (*c*) gradient Richardson number measured with a resolution of 10 m; and (*d*) TKE dissipation. Measurements taken from Moum, Caldwell & Paulson (1989).

is actively being forced by shear, however, the energy fed into the stratified layer is dissipated via breakdown of local instabilities by maintaining Ri_g at or below the critical value. In so doing, the internal wave energy of the stratified layer can be maintained within narrow limits. The possibility of maintaining a saturated wave field in the oceanic thermocline via a balance of energy input and dissipation has been hypothesized in developing a oceanic internal wave climatology model by Garrett & Munk (1972).

4.3. *Entrainment rate*

One of the macroscale effects of microscale mixing at the interface is the deepening of the upper turbulent layer, which is defined by the entrainment velocity u_e given by

$$u_e = \frac{\mathrm{d}D(t)}{\mathrm{d}t}. \tag{4.3}$$

This measurement requires accurate measurement of the mixed-layer depth $D(t)$ as it evolves in time, and more importantly an accurate estimation of its derivative with respect to time. The usual practice has been to record the depth evolution using dye visualization or conductivity probes and compute u_e using a best-fit of D versus t data. From figure 3(*a–h*), however, it is clearly evident that at low Ri_B the interface is highly convoluted (with disturbance sizes sometimes equaling 20% of D), which calls for suitable averaging rather than instantaneous measurements. Considering

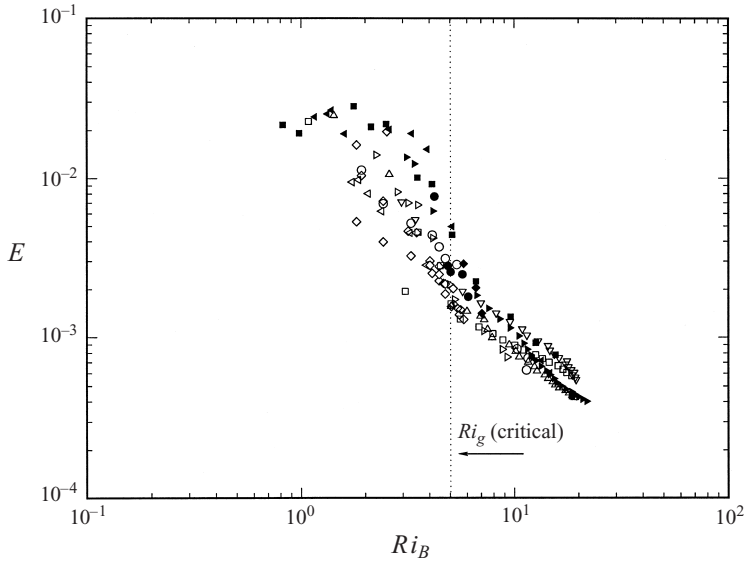

FIGURE 7. Dependence of entrainment coefficient E on Ri_B (solid symbols, two-layer case; open symbols, linearly stratified case).

the horizontal homogeneity of the problem, we have used spatial averaging in the streamwise direction to obtain the mean displacement of the interface. As discussed in § 3, LIF measurements of spatial density structure covering a horizontal scale of 8 cm were used; this averaging length is larger than the typical interfacial distortions of 1–5 cm.

Figure 7 presents measurements of the entrainment rate $E = u_e/\Delta U$ as a function of Ri_B for the present flow configuration. By inspection, it is possible to identify the following regimes in this diagram (some of these regimes have been noted by Fernando 1991, but no detailed mechanisms were discussed).

(*a*) Regime I: When $Ri_B < 1.5$ (or equivalently, $\overline{Ri}_g < 0.09$), the entrainment takes place as if no stratification were present, independent of Ri_B (or $\overline{Ri}_g$), and the entrainment law takes the form $E \simeq 0.024$. Here, the turbulent eddies in the shear layer are sufficiently strong to scour dense fluid against buoyancy forces. The data of figure 7 are consistent with those reported by Christodoulou (1986) which show $u_e/\Delta U \rightarrow 0.02 - 0.04$ at low Ri_B.

(*b*) Regime II: When $Ri_B > 1.5$ ($\overline{Ri}_g > 0.09$), E depends on Ri_B, but the data show considerable scatter in the regime $1.5 < Ri_B < 5$. In this regime, K-H billowing is the dominant mixing mechanism and K-H billows can exist by themselves ($Ri_B < 3.2$) or together with asymmetric waves ($3.2 < Ri_B < 5$). The exact power law dependence between E and Ri_B is highly variable among different experiments, leading to considerable scatter. A clear distinction, however, could be made between the two-layer and linearly stratified experiments, with the latter showing lower entrainment rates. This difference can be attributed to the radiation of energy into the lower stratified layer via internal waves, as will be discussed in detail in § 6. It is also interesting that the suppression of K-H type instabilities at $Ri_B > 5$ is associated with a reduction of the entrainment rate (by an order of magnitude), and the data for two-layer and linearly stratified cases collapse to some degree onto each other at $Ri_B > 5$ (although there

is still some positive bias toward the two-layer case). In summary, it appears that the internal wave radiation to the lower stratified layer is significant in the regime $1.5 < Ri_B < 5$ whence K-H billows are active.

It is instructive to note that the above findings are in agreement with limited observations that have been made in natural water bodies. For example, in their measurements in Pannikan Bay, which is an embayment of Lake Argyle in Western Australia, Zic & Imberger (2000) have noted rapid deepening of the surface mixed layer followed by slower deepening, when the surface wind forcing is sustained for several hours. Based on supplementary observations, they attributed the rapid deepening to K-H billowing events at the base of the mixed layer. Our measurements suggest that this second slow deepening may be due to the transition to a less effective mixing regime. Interestingly Zic & Imberger (2000) note that, during the rapid deepening (active K-H) period, the motion field below the mixed-layer base increased its amplitude to the extent of developing sporadic overturning events. This can be attributed to the leakage of energy from the base of the mixed layer by the radiating internal waves. Furthermore, they found that the lake mixed-layer model of Spigel, Imberger & Rayner (1986) consistently overestimated the mixed-layer depth (i.e. predicted high entrainment rates) during the rapid deepening phase, but performed well thereafter. The model of Spigel *et al.* (1986) does not account for the energy radiation by the internal waves and, hence, its overprediction of the entrainment rate during K-H events can be construed as due to neglecting internal wave radiation.

Another salient feature of Regime II ($1.5 < Ri_B < 5$) is the presence of a slight 'bump', especially for the two-layer case at $Ri_B \sim 3$–4 followed by a sharp reduction of E. This bump is a contributing factor to the larger exponent of decay for entrainment at the upper limit of Regime II ($n \sim 2$–3). The sharp reduction of E is particularly evident from the data of Lofquist (1960) and Deardorff & Willis (1982), though their measurement accuracy did not allow the resolution of this bump. A possible explanation for this bump is the efficient transport of buoyancy across the interface in the Richardson number regime $3 < Ri_B < 4$, which is described below.

As shown in figure 8(*a*), due to rapid local turbulent mixing by K-H billows, a time-dependent intermediate layer appears separating the dense lower and lighter upper layer fluids. The existence of this intermediate layer was also noted by Fernando (1986), Narimousa & Fernando (1987) and Sullivan & List (1994). Turbulent eddies carry partially mixed fluid from this layer to the fully turbulent upper layer, completing the entrainment. As such, the interfacial region shows periodic swelling due to K-H billowing and their degeneration to turbulence; this is followed by thinning due to encroachment of partially mixed fluid by eddies. At $Ri_B < 5$, the production rate of intermediate fluid exceeds its transport rate to the turbulent layer, and hence a well-defined intermediate layer with an average buoyancy frequency N_I can be identified.

Figure 8(*b*) displays data on the normalized intermediate-layer buoyancy frequency $N_I \delta_{bh}/w_{rms}$ as a function of Ri_B for $Ri_B \leqslant 5$. Here the buoyancy frequency N_I is vertically averaged across the intermediate layer and then streamwise averaged across the width of the illuminating laser sheet (measured using LIF). The normalizing frequency w_{rms}/δ_b is a characteristic of K-H billowing, based on the r.m.s. of vertical velocity fluctuations $w_{rms} = \overline{w^2}^{1/2}$ (measured using the hot film) and billow height δ_{bh} (recorded when the maximum vertical development of the billow was observed within the LIF procedure). It is clear that the two frequencies coincide with each other ($N_I \delta_{bh}/w_{rms} \simeq 1$) at $Ri_B \sim 3-4$, around which a maximum of the entrainment

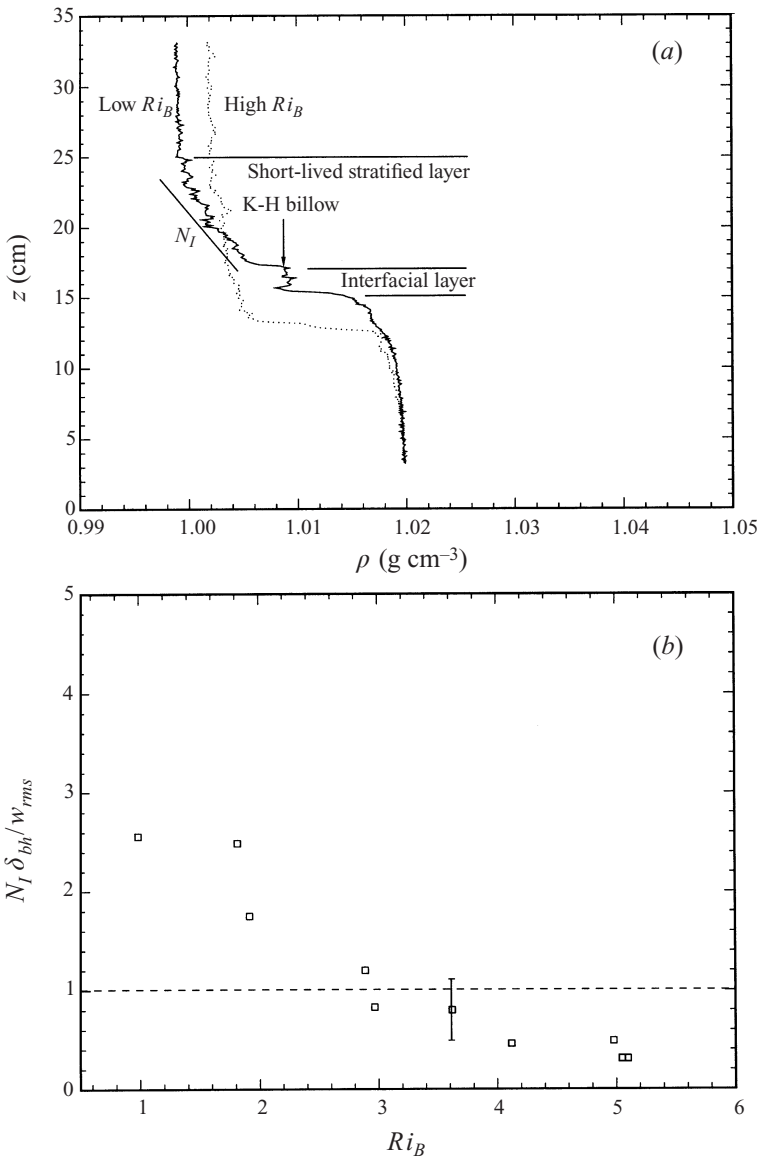

FIGURE 8. (*a*) Density structure identifying the instantaneous interfacial, intermediate and mixed layers (solid line, $Ri_B \sim 2.5$; dotted line, $Ri_B \sim 5.2$), and (*b*) variation of the ratio of the intermediate-layer buoyancy frequency normalized by the frequency characteristic of K-H billow growth $N_I\delta_{bh}/w_{rms}$ with Ri_B (two-layer case).

velocity occurs. Thus the enhanced entrainment occurs when the time scales of turbulent transport and buoyant production in the intermediate layer match with each other.

Our data suggest that, in Regime II the entrainment law takes the form

$$E \simeq C_2 Ri_B^{-n}, \tag{4.4}$$

where $C_2 \simeq 0.22 \pm 0.11$ and $n \simeq 2.63 \pm 0.45$ for the two-layer case. Conversely, $C_2 \simeq 0.08 \pm 0.02$ and $n \simeq 2.10 \pm 0.18$ for $0.7 < f_N < 1.8$, and $C_2 \simeq 0.03 \pm 0.02$ and

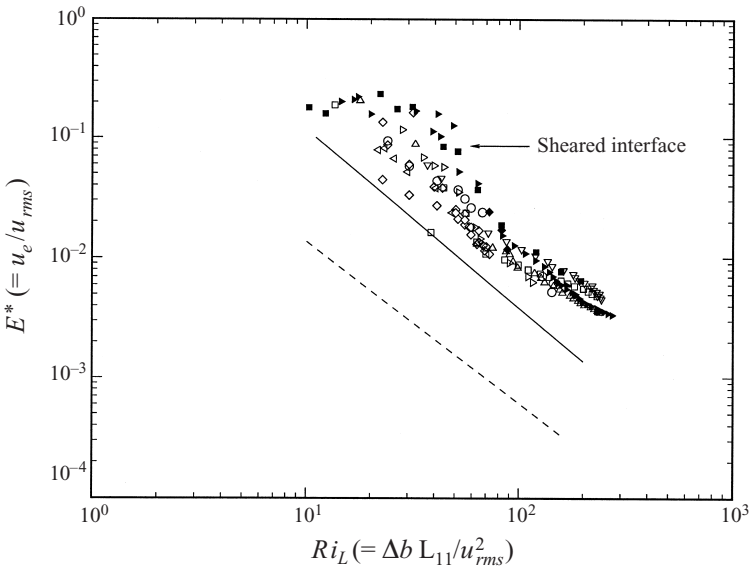

FIGURE 9. Dependence of re-scaled entrainment coefficient E^* on Ri_L (solid symbols, two-layer case; open symbols, linearly stratified case; solid line, shear-free data from E & Hopfinger 1986; dashed line from Perera, Fernando & Boyer 1994).

$n \simeq 1.59 \pm 0.38$ for $2.1 < f_N < 4.8$, indicating the effect of internal wave radiation in determining E. Note that (4.4) can be recast in terms of $\overline{Ri}_g$ by using $\overline{Ri}_g \simeq 0.038 Ri_B^2$; for example, for the two-layer case, (4.4) becomes $E \sim 1.20\overline{Ri}_g^{-1.3}$.

(*c*) Regime III: In some previous studies (Deardorff & Willis 1982; Narimousa & Fernando 1987), a regime dominated by interfacial 'wave breaking' has been identified for $5 < Ri_B < 20$. The present data shown in figure 7 clearly support the lower limit of this regime, where changes of the entrainment behaviour can be noted. In this regime, both two-layer and linearly stratified experiments approximately collapse onto the same curve, indicating insignificant energy loss due to internal wave radiation. The entrainment law for this regime ($5 < Ri_B < 20$) can be written as

$$E \simeq C_3 Ri_B^{-n}, \tag{4.5}$$

where $C_3 \simeq 0.02 \pm 0.01$ and $n \simeq 1.30 \pm 0.15$ for $f_N = 0$. Conversely, $C_3 \simeq 0.02 \pm 0.01$ and $n \simeq 1.20 \pm 0.38$ for $1.4 < f_N < 4.8$.

(*d*) Regime IV: Although the present results do not extend beyond Regime III, previous work has supported the existence of an (extremely slow) entrainment regime at $Ri_B > 20$ dominated by molecular-diffusive effects. This regime is further discussed in Fernando (1991).

In summary, the present results represent the most highly resolved entrainment measurements so far reported for stratified shear flows. For the two-layer stratification, the reported measurements are generally consistent with the laboratory experiments of Lofquist (1960) and Deardorff & Willis (1982), although their data are highly scattered for $Ri_B > 5$. Also, the present observations are consistent with those of Sullivan & List (1994) who noted that K-H billowing dominates the interfacial activity for $Ri_B < 5$ and intermittent wave breaking is prevalent for $Ri_B > 5$ in two-layer stratified shear flows.

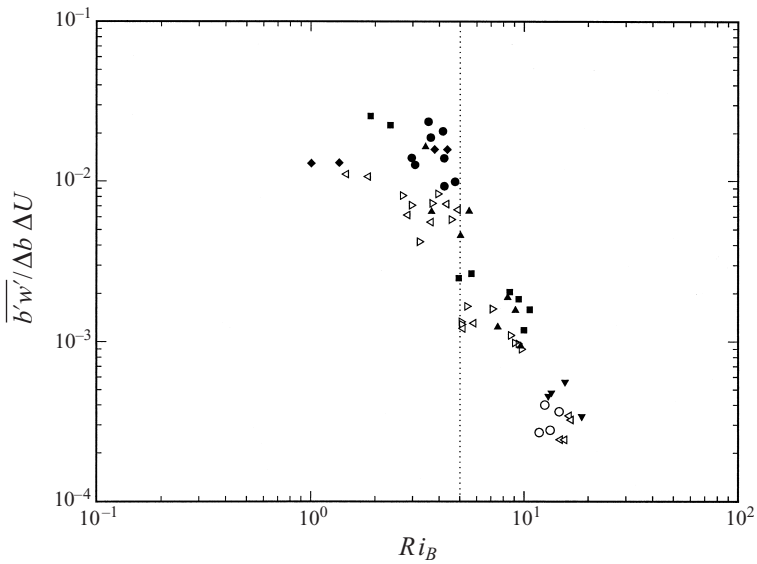

FIGURE 10. Temporally and spatially averaged interfacial buoyancy flux normalized by the interfacial buoyancy and velocity jumps $\overline{b'w'}/\Delta b\Delta U$ versus Ri_B (solid symbols, two-layer case; open symbols, linearly stratified case).

4.4. *Comparison with shear-free entrainment*

Using the relationships u_{rms} ($\simeq 0.12\Delta U$) and L_{11} ($\simeq 0.18D$), discussed in § 2, the entrainment data of figure 7 were re-scaled as $E^* = u_e/u_{rms}$ and $Ri_L = \Delta b L_{11}/u_{rms}^2$, and are shown in figure 9. These new variables facilitate the comparison of entrainment rates across a sheared density interface with that of the shear-free case. To this end, the shear-free experimental data of E & Hopfinger (1986) for a 'thin' density interface (solid line) and Perera *et al.* (1994) for a 'thick' interface (dashed line) are shown in figure 9. The shear-induced entrainment coefficient is more than a factor of two greater than the 'thin' interface data of E & Hopfinger (1986) and an order of magnitude greater than the 'thick' interface data of Perera *et al.* (1994). The presence of mean shear makes the interface susceptible to additional instabilities, such as K-H and Hölmböe waves, thus facilitating more efficient mixing.

5. Interfacial buoyancy flux

In support of the entrainment measurements and concepts presented in § 4.3, measurements of buoyancy flux are described here. The measurements were made using techniques described in § 3.2, and the normalized buoyancy flux measurements are presented in figure 10. Comparison of figure 10 (normalized buoyancy flux) and figure 7 (entrainment coefficient) show some noteworthy features, namely the normalized buoyancy flux exhibits a similar magnitude and dependence on Ri_B as the entrainment coefficient, and further, it exhibits the same disparity between the two-layer and linearly stratified cases as observed for the entrainment data.

The former observation can be understood by straightforward integration of the buoyancy conservation equation across the upper layer which, in the limit $\delta_s/D \to 0$, becomes

$$\left|\overline{b'w'}\right| \simeq \Delta b u_e, \tag{5.1}$$

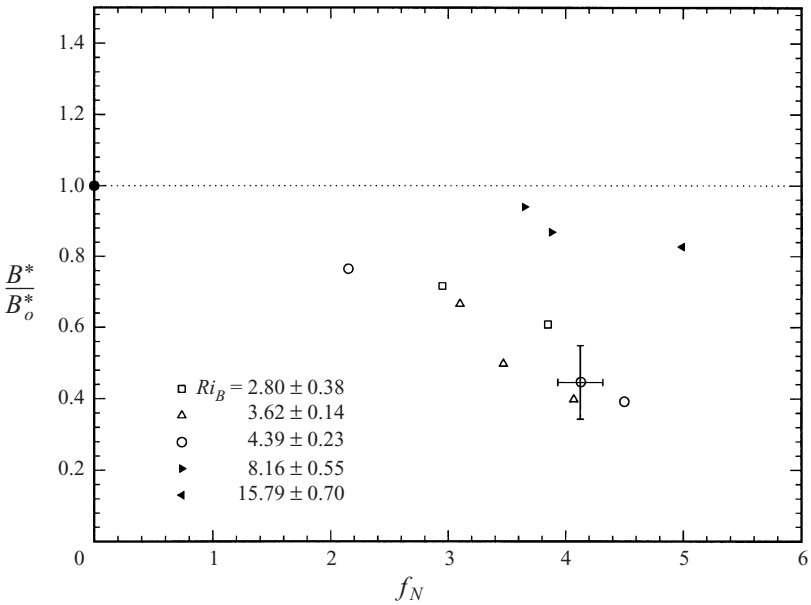

FIGURE 11. Buoyancy flux of linearly stratified experiments B^* normalized by B_o^* (two-layer case) versus the frequency ratio $f_N = ND/\Delta U$ (open symbols, K-H regime; solid symbols, symmetric Hölmböe wave regime).

and hence

$$E = \frac{u_e}{\Delta U} \simeq \frac{|\overline{b'w'}|}{\Delta b \Delta U}. \tag{5.2}$$

Comparison of figures 7 and 10 shows that the proportionality constant of (5.2) is 1.1 ± 0.25, indicating that the two independent measurements of E, one based on $\overline{b'w'}$ and the other based on direct measurements, are in excellent agreement within the error margins. This also testifies to the accuracy of our measurements.

The effects of internal wave radiation can be further evaluated by writing the normalized buoyancy flux B^* in the spirit of (2.6), namely

$$B^* = \frac{|\overline{b'w'}|}{\Delta b \Delta U} = g_1(Ri_B, f_N), \tag{5.3}$$

where $|\overline{b'w'}|/\Delta b \Delta U \to B_o^*(Ri_B)$ as $f_N \to 0$ (two-layer limit) and g_1 is a function. Thus, (5.3) becomes

$$\frac{B^*}{B_o^*} = g_2(Ri_B, f_N), \tag{5.4}$$

with $g_2 = 1$ for $f_N \to 0$. Figure 11 shows a plot of B^*/B_o^* versus f_N for different Ri_B values, representing different regimes. Note that, in the K-H regime ($1.5 < Ri_B < 5$; open symbols), there is a substantial reduction in the buoyancy flux in the linearly stratified case compared to the two-layer case, and this reduction increases with increasing f_N. Furthermore, within the experimental error, this reduction appears to be insensitive to Ri_B. In contrast, when $Ri_B > 5$, the reduction in the buoyancy flux from the two-layer case is much smaller. This is consistent with the discussion in § 4.3, wherein the entrainment coefficient for $1.5 < Ri_B < 5$ is characterized by reduced mixing when the deep layer is linearly stratified.

6. Internal waves

We noted that in Regime II ($1.5 < Ri_B < 5$), the respective entrainment rates and interfacial buoyancy fluxes for the two-layer case are noticeably larger than the linearly stratified case, and that the normalized interfacial buoyancy flux is strongly dependent upon f_N (given that the flow only depends on Ri_B and f_N, at a given Ri_B, the difference between the two cases arises due to the deep-layer stratification in the latter case where $f_N \neq 0$). Therefore, a possible reason for the disparity is the removal of energy available for mixing at the interface by internal waves radiating into the deep layer. This aspect is discussed below by identifying internal wave generation mechanisms and estimating the amount of energy radiated.

Since the disparities of entrainment rates for the two cases occur in the regime dominated by K-H billows, it is possible to surmise that K-H billowing is intimately connected with the internal wave generation. The linear internal wave theory suggests that for internal waves to propagate out from the interface, the wave frequency ω should be smaller than the buoyancy frequency N of the bottom layer. After careful considerations, several internal wave excitation sources could be identified and discriminated by whether they can contribute to internal wave generation, namely:

(*a*) The frequency associated with the passage of individual K-H billows, where typical wavelengths of the billows are several centimetres (i.e. 2–3 cm) with advection speeds of approximately $u \sim 5\,\mathrm{cm\,s^{-1}}$, hence, an excitation frequency of $\omega \sim 2.5$ ($\mathrm{rad\,s^{-1}}$) can be expected for this case. This is too high of a frequency to excite internal waves, given that $0.5 < N < 1.25\ \mathrm{rad\,s^{-1}}$.

(*b*) The turbulence generated by the breakdown of billows, having a r.m.s. velocity w_{rms} and a vertical scale $\delta_{bh} = 0.22\Delta U^2/\Delta b$ (determined by inspection of LIF results) can be considered as an energetic internal wave exciting mechanism (this is expected to overshadow the contributions from the turbulence in the upper mixed layer). However, as evident from figure 8(*b*), over part of the Ri_B range where wave radiation is active, $w_{rms}/\delta_{bh} \sim N_I$. In the range $1.5 < Ri_B < 5$, the ratio N_I/N tended to be close to or higher than unity, hence, $w_{rms}/\delta_{bh} \geqslant N$. As such, the wave radiation by this mechanism is less likely at moderate N. Even at higher deep-layer stratification, the phase velocity of the excited waves is mainly horizontal and, hence, the group velocity is nearly zero. Therefore, it is hard to expect significant leakage of wave energy into the bottom layer by this mechanism.

Therefore, it is necessary to investigate further the morphology of the entrainment for $1.5 < Ri_B < 5$ to identify sufficiently low-frequency events capable of exciting deep layer internal waves. In figure 12(*a*), a time trace of the spatially averaged interfacial buoyancy layer thickness $\delta_b(t)$ is presented. With the progression of time, the average Richardson number (both locally and globally defined) increases. At $t \sim 460\,\mathrm{s}$, the bulk Richardson number Ri_B is at approximately the critical value, i.e. $Ri_B \sim 5$. Moreover, $t < 460\,\mathrm{s}$ (in this figure) corresponds to interfacial behaviour consistent with Regime II. Simply from inspection of figure 12(*a*), it is immediately apparent that an approximately periodic low-frequency modulation of the interfacial thickness occurs when $1.5 < Ri_B < 5$. An expanded view of the time trace of figure 12(*a*) replotted in figure 12(*b*) (for $240 < t < 500\,\mathrm{s}$), shows that the interfacial modulation ('swelling' and 'thinning') occurs with a period of 20–30 s; in fact, the time duration between 'swelling' events increases with Ri_B and, therefore, increases with time in an experiment. These 'swelling' events are certainly of a frequency (and, as will be determined later, amplitude) to force internal wave propagation in the deep stratified layer.

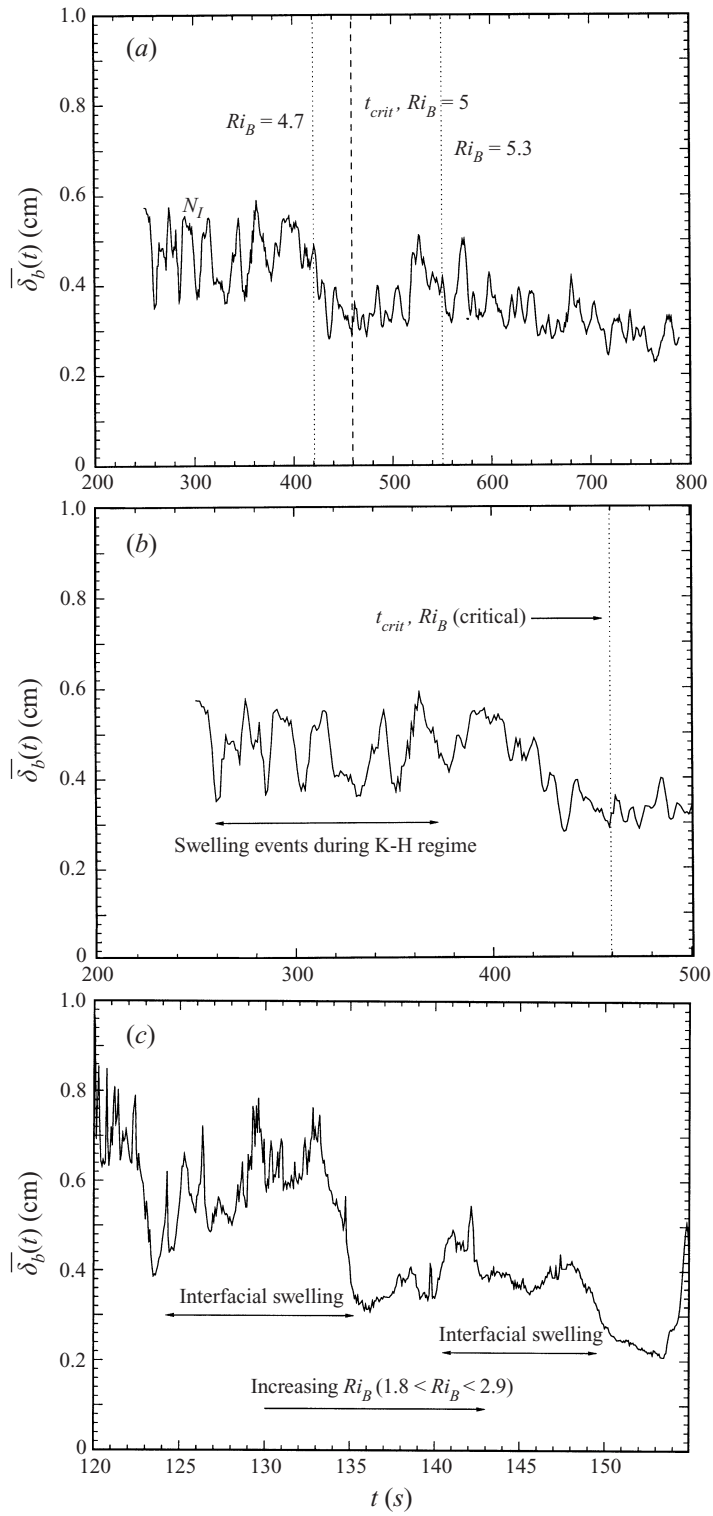

FIGURE 12. Temporal variation of the spatially averaged thickness of the density interface for the following: (*a*) transition across the critical Ri ($3.5 < Ri_B < 6.2$); (*b*) enlarged region of prior figure; and (*c*) early stages of K-H regime ($1.8 < Ri_B < 2.9$).

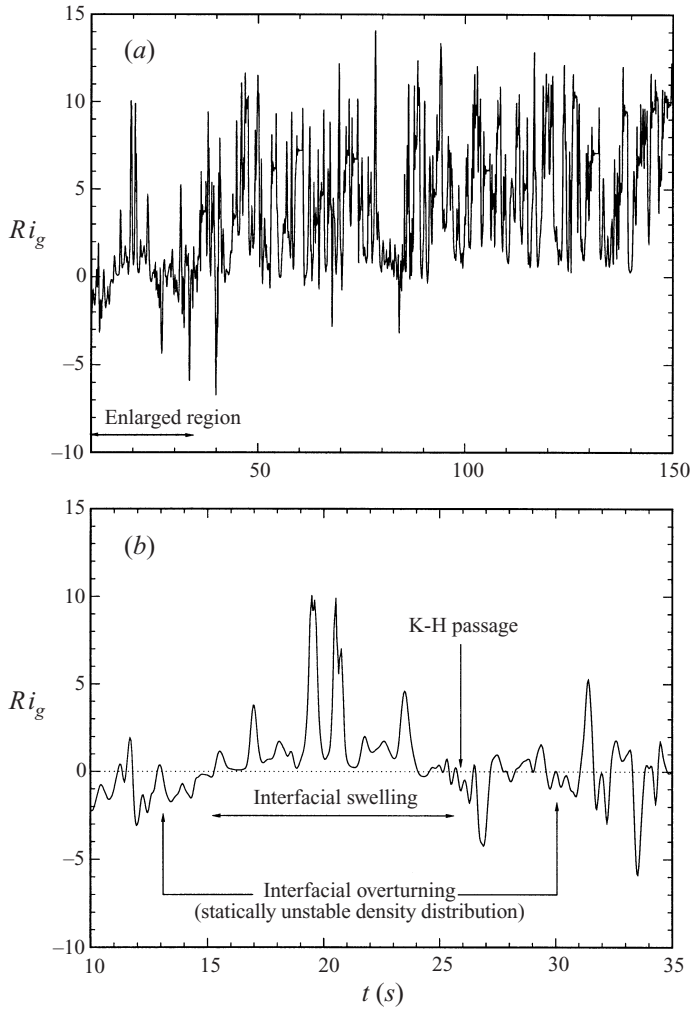

FIGURE 13. Temporal variation of local gradient Richardson number Ri_g measured across the interfacial and intermediate layer: (*a*) Non-stationary time-trace ($2.7 < Ri_B < 3.3$); (*b*) enlarged region extending from 10 to 35 s.

On a finer time scale, figure 12(*c*) presents an additional time trace of the interfacial buoyancy layer thickness for $1.5 < Ri_B < 3$. Due to the range of Ri_B spanned in this time trace, the entrainment rate is relatively high and the interfacial buoyancy layer thickness gradually thins over a time scale on the order 20 s. From the times of 124 to 135 s and 140 to 150 s, interfacial swelling occurs, which can be attributed to the recurrence of K-H billows, a phenomenon that has been conjectured by Spigel *et al.* (1986) based on limnological observations (also see Zic & Imberger 1999). Although their measurements hinted at the existence of interfacial swelling, no true verification of this phenomenon has been made. In their numerical model of the diurnal mixed layer, Spigel *et al.* (1986) included this swelling/thinning as a controlling mechanism of mixed-layer deepening. The present observations provide the first convincing evidence for this phenomenon.

Consider the interfacial thickness at time 124 s to be nominally thin (figure 12*c*). At

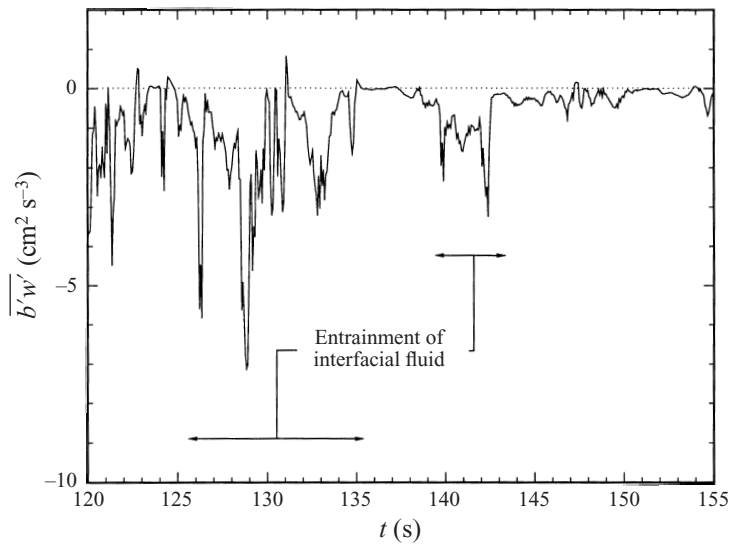

FIGURE 14. Temporal variation of the spatially averaged interfacial buoyancy flux; the time axis is the same as that of figure 12(c) ($1.8 < Ri_B < 2.9$).

this moment, the local gradient Richardson number falls below a critical value leading to K-H instability. The passage of K-H billows is signified by periodic (high-frequency) oscillations of Ri_g, which is expected to become negative when overturning motions (inversions) are present. The collapse of billows promotes interfacial turbulence and local mixing, leading to the thickening of the interface. Simultaneously, Ri_g increases as a result of the smearing of the local density and velocity gradients (increase of density and velocity scales). These trends in Ri_g are clearly observed in the measurements shown in figure 13(a, b) which do not directly correlate with figure 12(c), but are characteristic of the K-H regime.

Figure 13(a) is a time trace of Ri_g measured across the interface and shear layer. This measurement was performed by placing the Ri_g probe below the interface and recording the signal as the interface passes (thus exploiting the transient nature of the experiment). The time trace is very irregular with significant variability. The spectrum of scales which influences this measurement is large, including the spectral ranges of waves and turbulence. Additionally, there is temporal variability due to the transient nature of the deepening process and spatial inhomogeneity in the vertical direction. Figure 13(b) is a portion of figure 13(a) extending from the time of 10 to 35 s that includes an interfacial swelling event. Ri_g takes negative values indicating overturning activity! As indicated in the figure, the oscillations during the span of time from 10 to 15 and 25 to 30 s can be attributed to the passage of K-H instabilities developed upstream of the measurement location. At these times, negative values of Ri_g occur because of overturning. For the range $1 \leqslant Ri_B \leqslant 5$, the period of oscillations is approximately 1 s.

The observed re-thinning of the interface following swelling events can be attributed to the erosion of partially mixed fluid in the swelled region by the scouring motions of the eddies, which also generates a buoyancy flux. Figure 14 presents a time trace (concurrent with figure 12c) of the spatially averaged interfacial buoyancy flux. Clearly, during the times of interfacial swelling, the buoyancy flux is negative, representing an upward transport of heavy fluid across the interface and completion

of an entrainment cycle following a billowing event. This trend for interfacial activity recurs at least until K-H instability subsides significantly around $Ri_B \simeq 5$. Moreover, for brief periods (or 'spikes') of time the buoyancy flux is positive signifying the overturning and collapse of K-H instability.

In summary, the low-frequency events associated with interfacial swelling (or the breakdown of a group of K-H billows), was found to have a typical intrinsic frequency of 0.19–0.63 rad s^{-1} ($< N$), an amplitude of the order δ_{bh}, and could be considered a plausible internal wave excitation mechanism for the deep stratified layer. Further calculations demonstrated that the magnitude of entrainment loss observed in figure 7 is consistent with this mechanism of internal wave radiation, as discussed below.

It should be noted that the passage of K-H billows occupies a large vertical extent within the interfacial layer. In essence, they roll up a significant portion of interfacial fluid and force the deep-layer stratification with a relaxation time equivalent to that of interfacial swelling. Following Linden (1975), it is possible to estimate the ratio of the wave energy flux to the rate of change of the potential energy due to mixed-layer deepening as

$$\mathrm{IWR} = \frac{4}{3\pi\sqrt{3}} \frac{A^2 \lambda N}{\left[(D^2 - D_o^2) + 2\Delta b_o D_o / N\right] u_e}, \tag{6.1}$$

where λ is the interfacial disturbance wavelength, A is the wave amplitude and N is the Brünt–Väisälä frequency. The amplitude of the interfacial wave disturbance A is proportional to the billow height $\delta_{bh} \simeq 0.22\Delta U^2/\Delta b$ and the typical wavelength λ of K-H induced swelling can be taken as approximately 30 cm for a deep-layer buoyancy frequency of $N \sim 1.0$ rad s^{-1}. These, together with u_e for $Ri_B \sim 4$, obtained from figure 7, can be used to calculate IWR $\sim 48\%$. The energy radiation by internal waves is quite significant for long wavelengths and is consistent with the changes of entrainment velocities observed in figure 7. Keep in mind the sensitivity of IWR to the buoyancy frequency N: when, $2\Delta b_o D_o / N \gg (D^2 - D_o^2)$, it is possible to write IWR $\propto N^2$, and this trend is borne out by the measurements shown in figure 11.

The above IWR estimates are close to those of Kantha (1977) and Kantha *et al.* (1977) based on their mixed-layer deepening observations in stratified shear flows and by Linden (1975) for shear-free cases. In the oceanic context, Dillon *et al.* (1989) noted that, based on their observations in the Tropic Heat Experiment, the zonal momentum balance in equatorial oceans cannot be realized without accounting for the radiation of internal waves from the base of the mixed layer.

A question arises as to the fate of the internal waves radiating from the mixed-layer base; the energy so radiated can dissipate by viscous effects, or it can reflect back from the bottom walls toward the interface. Townsend (1966) showed that the critical distance required for the dissipation of propagating waves by viscosity is given by $z_c = C\lambda^3 N/\nu$, where the constant C was experimentally found by Linden (1975) to be $C = 1.5 \times 10^{-3}$. For the present experiments with $\lambda \sim 30$ cm and $N \sim 1$ rad s^{-1}, $z_c \sim 4$ m, indicating that the radiated energy is reflected back and may interfere with the interface. Continuous reflection of these waves from the walls and interface is possible, with the possibility of building of energy and wave breaking in the lower layer when wave amplitudes become large (Orlanski & Bryan 1969). Since no drastic increases of the bottom layer r.m.s. buoyancy fluctuations were recorded over time, it is possible to conclude that the internal waves dissipate in the lower layer rather quickly, perhaps due to continuous reflection. In the case of oceans, it has been reported that the waves radiating from the mixed-layer base may dissipate by interacting with the mean shear (i.e. critical-layer absorption; Wijesekera & Dillon

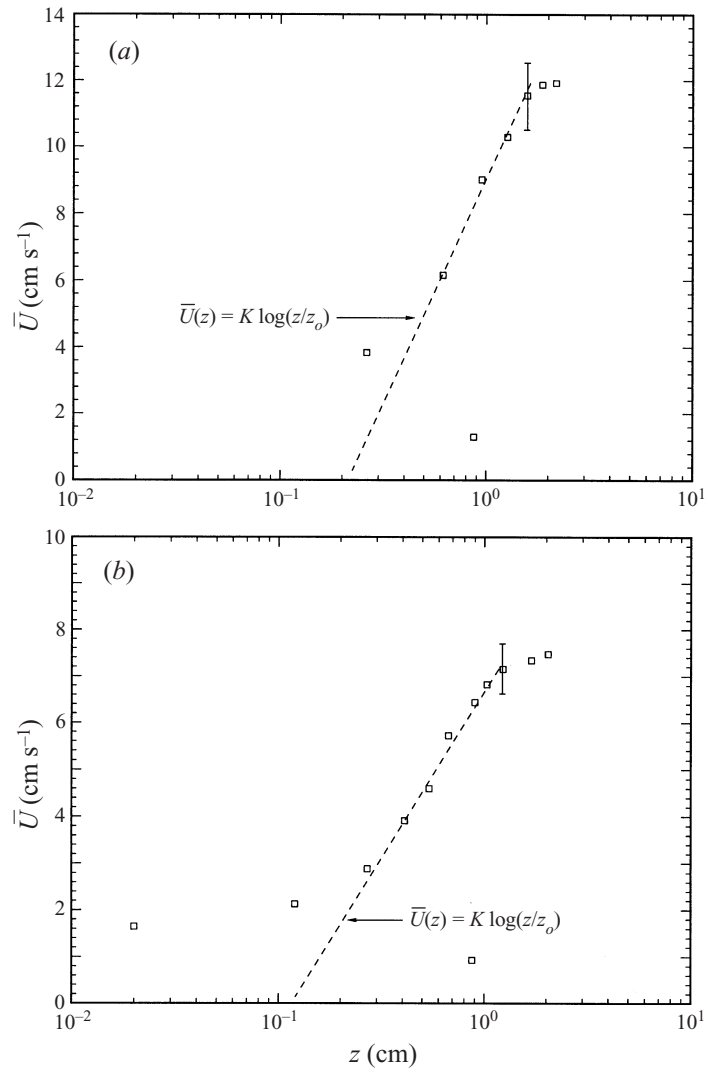

FIGURE 15. Semi-log plot of the mean streamwise velocity u as a function of distance from the interfacial layer centre z: (*a*) $Ri_B = 3.5$, (*b*) $Ri_B = 12.1$; two-layer experiments.

1991), but in the present case this mechanism is untenable due to lack of mean shear in the bottom layer.

7. Velocity structure in and near a density interface

As described in § 3, a two-component hot-film probe placed next to a micro-scale conductivity sensor at a separation of 0.1 cm was used to record velocity and density profiles through the interface and the mixed layer. Velocity profiles so taken are shown in figure 15(*a*, *b*) for experiments carried out at $Ri_B \simeq 3.5$ and $Ri_B \simeq 12.1$, respectively. At lower Ri_B (in particular, $Ri_B < 3$), the measurement of such profiles is difficult, as the interface deepens at substantial rates. The profiles shown are plotted on a semi-log graph in order to check the 'law of the interface' proposed by Csanady

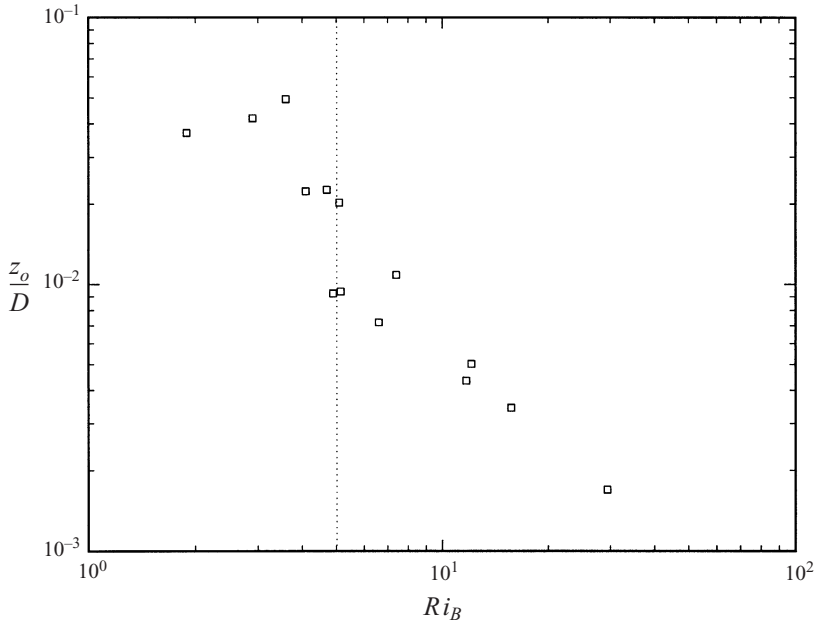

FIGURE 16. Interfacial roughness height normalized by the mixed-layer depth z_o/D as a function of Ri_B (two-layer case).

(1978). Accordingly, the velocity profiles near a sharp density interface should be logarithmic,

$$\overline{U}(z) = K \ln\left(\frac{z}{z_o}\right) = \frac{u_*}{\kappa} \ln\left(\frac{z}{z_o}\right), \tag{7.1}$$

where z is the distance measured through the centre of the interface into the mixed-layer, $K = u_*/\kappa$ is the slope of the log-layer given by the ratio of the interfacial friction velocity u_* to the von Kármán constant $\kappa = 0.41$, and z_o is the virtual origin or interfacial 'roughness height'. A good agreement over a range of z can be noted (dashed lines). As in the work of Charnock (1955) on velocity profiles over wind-driven surface waves, the interfacial roughness height z_o can be calculated by determining the virtual origin of figure 15(a, b); simultaneously the friction velocity u_* can be evaluated by determining the slope.

The non-dimensional interfacial roughness height as a function of Ri_B is shown in figure 16. The available data suggest that when $Ri_B < 5$, the normalized roughness height is slowly varying, perhaps as $z_o/D \sim Ri_B^{-1}$, proportionately to K-H billow heights at their collapse (however, available data were not sufficiently extensive to formally support this notion). At larger values of Ri_B (> 5), z_o/D decreases as $z_o/D \sim Ri_B^{-1.4}$. Sullivan & List (1993) also attempted to fit their stratified shear layer data to (7.1), but the results were inconclusive because of the limited amount of data available and the scatter, though some support for (7.1) could be seen.

Figure 17 shows the variation of $u_*/\Delta U$ with Ri_B. It appears that $u_*/\Delta U$ increases until about $Ri_B \simeq 3$, and then starts decreasing; however, this is inconclusive due to the lack of data at low Ri_B. Best fit lines to the data in figure 17 indicate that $u_*/\Delta U \propto Ri_B^{n_1}$ with $n_1 \sim -1.0$ for $3 < Ri_B < 5$ and $n_1 \sim -0.5$ for $Ri_B > 5$.

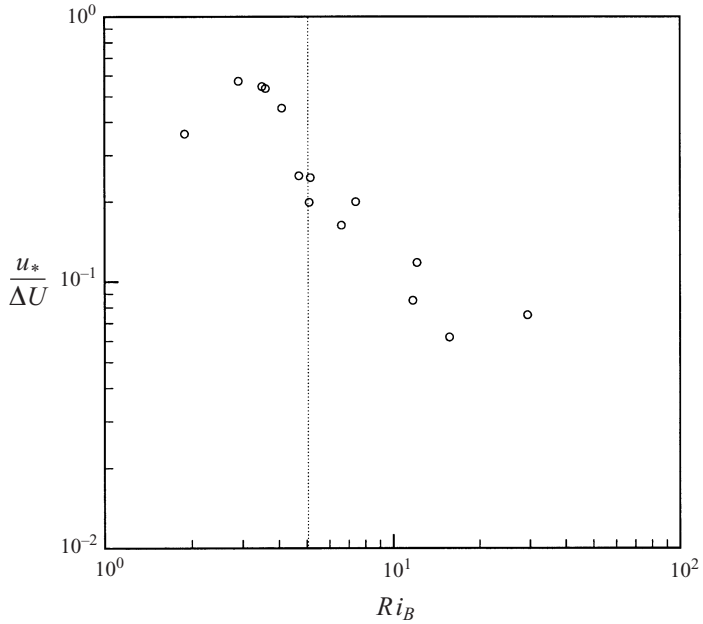

FIGURE 17. Interfacial friction velocity normalized by the interfacial velocity jump $u_*/\Delta U$ as a function of Ri_B (two-layer case).

8. Turbulent kinetic energy (TKE) budget

The mixed-layer deepening of our experiment is driven by the TKE generation by the mean shear, which in turn is expended in working against buoyancy forces to raise the potential energy of the fluid column and for TKE dissipation. The relative importance of these processes can be determined by examining the TKE equation.

Neglecting viscous diffusion and assuming the flow is horizontally homogeneous, the TKE equation can be reduced to

$$\frac{\partial(\overline{q^2/2})}{\partial t} = P + B - \frac{\partial}{\partial z}\left[\overline{w'\left(\frac{p'}{\rho_o} + \frac{q^2}{2}\right)}\right] - \epsilon, \tag{8.1}$$

where P is the shear production, B is the buoyancy flux, ϵ is the rate of TKE dissipation, and the first and third terms represent the rate of change of TKE and the energy flux divergence. Assuming a quasi-stationary state of equilibrium (see § 3.4) and integrating (8.1) vertically across the mixed-layer depth, one obtains

$$0 = \int_0^D P\,\mathrm{d}z + \int_0^D B\,\mathrm{d}z - \int_0^D \epsilon\,\mathrm{d}z - \left[\overline{w'\left(\frac{p'}{\rho_o} + \frac{q^2}{2}\right)}\right]\Bigg|_{z=0}^{z=D}, \tag{8.2}$$

where the limits of integration have been chosen such that $z = 0$ is located at the isopycnal that defines the centre of the interface (in an averaged sense) and $z = D$ represents the mixed-layer free surface where the flux divergence term is zero. However, due to experimental limitations, the measurement of ϵ, B and P across the entire mixed-layer depth was not possible, and therefore they were measured from the centre of the interfacial layer ($z = 0$) to a vertical distance D^* where the flux divergence term in (8.2) can be considered negligible. In fact, mid-way through the mixed layer, the turbulence was found to be approximately isotropic, satisfying this

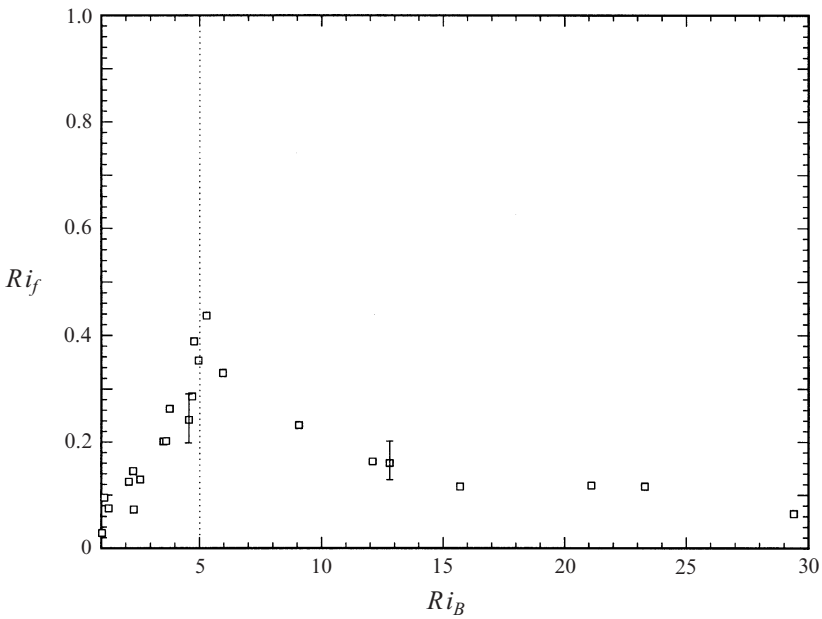

FIGURE 18. Variation of flux Richardson number Ri_f with Ri_B (two-layer case).

requirement. The same provisos cannot be applied to the lower limit of the integration, in particular when the lower layer is linearly stratified. Here, $p'w'$ can be substantial, indicative of the energy input to internal waves propagating from the base of the mixed layer. The TKE budget, however, was evaluated only for the two-layer case owing to the problems encountered in using the hot-film probe within the interface of the linearly stratified case. In the two-layer case, the TKE flux across $z = 0$ represents the energy flux used to generate irrotational motions in the lower layer and mixing in the lower part of the interfacial layer.

Neglecting the energy flux divergence term entirely and assuming quasi-stationarity, the depth-averaged TKE can be written as

$$0 \sim \bar{P} + \bar{B} - \bar{\epsilon}, \tag{8.3}$$

where the overbar denotes the depth-averaged quantities, e.g. $\bar{P} = (1/D^*)\int_0^{D^*} P\,\mathrm{d}z$. These quantities can be used to obtain useful information on interfacial energetics by calculating quantities such as the flux Richardson number (or the mixing efficiency) $Ri_f = -\bar{B}/\bar{P}$ and the TKE budget parameter $\alpha = (-\bar{B} + \bar{\epsilon})/\bar{P}$ that can be used to assess the degree to which the balance in (8.3) is valid.

Figure 18 shows the calculated Ri_f as a function of Ri_B. Note the shape of the curve. For $Ri_B < 2$, $Ri_f < 0.15$ indicating rather inefficient mixing. In the bulk of the K-H regime $1.5 < Ri_B < 5$, the mixing efficiency is higher, in particular at $Ri_B \sim 4$–6 wherein K-H billows and wave-like disturbances resonate causing internal mixing. Also this is the regime in which the buoyancy fluxes generated by local mixing are efficiently transported by eddies, as described in §4.3 (the time scales of generation and transport were the same).

Note that, although the most effective entrainment (largest E) occurs at $Ri_B \sim 3$–4, the maximum mixing efficiency occurs at $Ri_B \sim 5$. This is due to the fact that at $Ri_B \sim 5$ the interfacial production and eddy transport (to the upper layer) of mixed

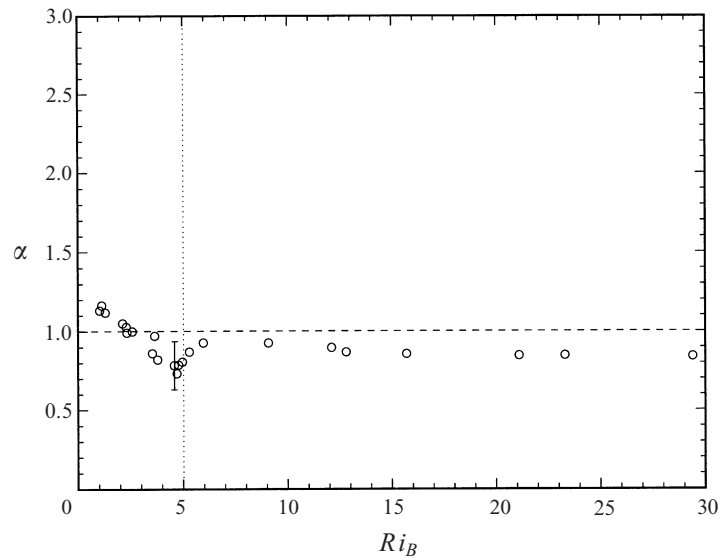

FIGURE 19. Variation of TKE budget parameter α with Ri_B (two-layer case).

fluid balance each other, as evident by the disappearance of the intermediate layer. When $Ri_B < 5$, the interfacial production dominates, leading to a thicker intermediate layer, with the rate of entrainment limited by the transport rate capabilities of mixed layer eddies. When $Ri_B > 5$, mixed-layer eddies can transport away more locally mixed fluid than is produced at the interface, with the rate limiting step being local interfacial mixing.

The TKE budget parameter α is shown in figure 19 as a function of Ri_B. A true balance between $\bar{P}$, $\bar{\epsilon}$ and $\bar{B}$ is indicated by a value of unity according to (8.3). The results show that for $Ri_B > 5$ or so, the energy balance can be reasonably represented by $\bar{P} + \bar{B} - \bar{\epsilon} \sim 0$ in that $\alpha \simeq 0.85$. The flow is quasi-stationary in this regime, as discussed in detail by Strang (1997), and the flux divergence term appears to have a noticeable but not significant contribution to the integrated energy budget.

For $3 < Ri_B < 5$, the α parameter tends to drop (at times as low as 0.5) indicating the possible significance of TKE fluxes at $z = 0$ and/or D^* and the non-stationarity of the interfacial region. Careful evaluation of the time traces of velocity indicate that the time-dependent term in (8.1) is not significant in this region (Strang 1997), and hence fluxes at $z = 0$ and/or D^* are mainly responsible for low α. Since the energy flux at $z = D^*$ still remains small due to the nearly isotropic nature of turbulence there, it is plausible that the energy leakage through $z = 0$ is responsible for the reduction in α. This notion is corroborated by the fact that α is a minimum in the range $3 < Ri_B < 5$. It is in this Ri_B range that the interaction between K-H billows and asymmetric waves leads to enhanced leakage of energy flux through $z = 0$.

In the case of a two-layer fluid, the above leakage tends to enhance mixing in the lower part of the interface. If the deep layer is linearly stratified, part or all of this leakage energy could have radiated as internal waves. The data of figure 7 are consistent with the above conjecture, and show enhanced entrainment (a 'bump' in E) for $3 < Ri_B < 4$ for the two-layer case and markedly reduced entrainment for the linearly stratified case.

If $F_o = -\overline{w'(p'/\rho_o + q^2/2)_{z=0}/D}$, then (8.2) takes the form $0 \simeq \bar{P} + \bar{B} - \bar{\epsilon} - F_o$,

where $F_o > 0$. The energy flux leaking through $z = 0$ can thus be evaluated as $F_o = (1-\alpha)\bar{P} = (1-\alpha)Ri_f^{-1}\bar{B}$. Note that when $\alpha = 1/2$, the TKE flux leaking through the middle of the interface is about half of the available TKE production for mixing. In the case of the homogeneous bottom layer, most of F_o can be utilized for additional mixing in the bottom half of the interfacial layer, whereas in the linearly stratified case F_o is lost through internal waves.

Lastly, when $Ri_B < 3$, α increases and eventually exceeds unity. This can be attributed to the non-stationarity of the interface, as indicated by time trace measurements of velocities (Strang 1997). Owing to substantial interfacial deepening during nominal sampling intervals, multiple measurements across the interfacial layer in a quasi-stationary sense are not accurate during this period. Therefore, it is imperative that one looks at the data at low Ri_B ($Ri_B < 2$) with circumspection.

9. Concluding discussion

A comprehensive research programme aimed at understanding the penetration of a shear-driven turbulent layer into an underlying dense (either homogeneous or linearly stratified with buoyancy frequency N) non-turbulent layer is described in the previous sections. Laser-induced fluorescence, laser-Doppler, acoustic-Doppler and hot-film anemometry, and conductivity measurements were used to obtain a unique set of data; to our knowledge, these are the most highly resolved entrainment measurements in stratified fluids gathered hitherto. The upper layer (of thickness D) was driven over the lower layer by a disk pump, as was done in several previous experiments. After some time from the start of the experiment, the flow assumed the configuration shown in figure 1. Here the density interface (of thickness δ_b and across which the buoyancy jump is Δb) is embedded in a thick velocity shear layer (of thickness δ_s and velocity jump ΔU) with the centre of the density interface offset by a distance d from that of the velocity interface. Based on dimensional and physical arguments, it was shown that the important governing parameters for the problem are the bulk Richardson number ($Ri_B = \Delta b D/\Delta U^2$) and the frequency ratio ($f_N = ND/\Delta U$). The upper part of the mixed layer is maintained in turbulent state by wall-induced turbulence and turbulence in the lower part is contributed by the turbulent production at the stratified shear layer (as discussed by Narimousa & Fernando 1987). The properties of turbulence in the mixed layer, therefore, are determined by ΔU and D. For example, the integral length scale L_{11} and the horizontal (vertical) r.m.s. velocity in the middle of the mixed layer u_{rms} (w_{rms}) were found to be $L_{11} = 0.18D$, $u_{rms} = 0.12\Delta U$, and $w_{rms} = 0.1\Delta U$.

The Richardson numbers used in the experiments were sufficiently large ($Ri_B > 1$) that the usual eddy-engulfment mechanism, which is typical of unstratified flows, was not applicable. Since the eddies were too feeble to scour dense fluid from across the interface into the upper layer, the entrainment occurred by local mixing induced by interfacial instabilities that caused the development of an intermediate layer of partially mixed fluid which, in turn, could be engulfed by turbulent eddies. As such, the instabilities at the interface and associated buoyancy flux, the transport of intermediate-layer fluid by turbulent eddies and its homogenization in the upper layer play crucial roles in the mixed-layer deepening process. The first two processes were identified as rate-limiting steps, depending on Ri_B.

Although interfacial disturbances are of finite-amplitude nature, linear stability results could be successfully used to identify interfacial instabilities. Linear stability analysis of the present flow configuration (widely different δ_s and δ_b, $\delta_b \neq 0$, $d \neq 0$

and D finite) has not been reported, but the related case of $\delta_s \neq \delta_b$, $d \neq 0$, finite D and $\delta_b = 0$ has been documented by Haigh & Lawrence (1999). When $D > 5\delta_s$, they identified the shear-layer Richardson number $Ri_s = \Delta b \delta_s / \Delta U^2$ and $e = d/\delta_s$ as the governing parameters. For the present case, both Ri_s and e are determined by Ri_B and f_N. Haigh & Lawrence (1999) predict instabilities for all Ri_s, but they conjecture that neither pure K-H nor Hölmböe waves may be observable for $e \neq 0$, which should be contrasted with the $e = 0$ case where a distinct transition from K-H to Hölmböe modes is predicted at $Ri_s = 0.046$. In the present experiments, nonetheless, for $Ri_s < 0.36$ (or $Ri_B < 3.2$, $\overline{Ri}_g < 0.39$) the predominant mode was K-H whereas Hölmböe modes dominated at $Ri_s > 0.64$ (or $Ri_B > 5.8$, $\overline{Ri}_g > 1.3$) irrespective of f_N. Here $\overline{Ri}_g$ is the averaged gradient Richardson number. Perhaps the most interesting regime is $3.2 < Ri_B < 5$, where both K-H and wave-like instabilities co-exist, possibly resonating with each other. These waves resemble one-sided asymmetric Hölmböe instabilities found in previous work. The mixing efficiency (or the flux Richardson number) peaked in this regime, with a maximum of 0.4 at $Ri_B \sim 5$. The wave asymmetry decreases with increasing Ri_B over the range $5 < Ri_B < 5.8$ and at $Ri_B > 5.8$ two-sided Hölmböe instabilities become dominant. There was an order of magnitude reduction in the entrainment rate beyond $Ri_B = 5$, at the transition from the active K-H/wave breaking regime to the (intermittently breaking) asymmetric wave regime. This suggests that practical mixed layer models can use $Ri_B \sim 5$ or $\overline{Ri}_g \sim 1$ as the threshold beyond which there is negligible mixed-layer deepening.

In $1.5 < Ri_B < 5$, when K-H instabilities are present, the entrainment law could be represented by $E \simeq 0.22 Ri_B^{-2.6}$ for the two-layer case and $E \simeq 0.076 Ri_B^{-2}$ ($0.7 < f_N < 1.8$) or $E \simeq 0.033 Ri_B^{-1.6}$ ($2.1 < f_N < 4.8$) for the linearly stratified case. In general, our results did not confirm the model proposed by Hannoun & List (1988) for the K-H regime wherein $E \sim Ri_B^{-2}$ nor did they agree with some previous experimental results reviewed in Fernando (1991). A possible reason is the high resolution of the present measurements that enabled capturing of the detailed variation of D. Furthermore, one of the fundamental assumptions made in the mixed-layer model of Pollard *et al.* (1973) that Ri_B is maintained constant during entrainment, obviously, was not borne out by our measurments. When asymmetric waves or symmetric Hölmböe waves are dominant at $Ri_B > 5$, the entrainment law followed $E \simeq 0.02 Ri_B^{-1.3}$ for the two layer case and $E \simeq 0.02 Ri_B^{-1.25}$ ($1.4 < f_N < 4.8$) for the linearly stratified case, indicating approximately similar behaviour. This contrasts with the observations in the K-H regime wherein, for a given Ri_B, the entrainment rate for two-layer fluids can be a factor of two higher. The internal wave radiation from the base of the mixed layer was attributed to this observation.

Detailed energy budget and interfacial observations revealed some interesting aspects of internal-wave radiation. Considering a number of possibilities for the excitation frequency, for example those corresponding to mixed-layer eddies, advection of K-H billows and the range of frequencies induced by secondary instabilities of K-H billows, it was concluded that the most viable internal-wave excitation source is the interfacial swelling events. Locally mixed fluid generated by interfacial instabilities causes the interface to swell, leading to an intermediate layer sandwiched between the interfacial layer and the upper mixed layer, which, in turn, is eroded by the mixed-layer eddies to generate a low-frequency event (of the order 0.25–0.5 Hz in the present case). The ensuing thin interface again becomes unstable, causing K-H billowing and swelling. The recurrence of these events acts as the excitation source of internal waves. When $Ri_B < 5$, the production rate of intermediate-density fluid

is faster than or of the same order as its removal by the eddies and thus the intermediate layer is well defined. Estimation of internal-wave radiation based on the frequency of the swelling phenomenon is consistent with that evaluated by the direct measurement of the energy budget. At $Ri_B > 5$, the intermediate layer can hardly be detected, implying that the rate of buoyancy transport by the eddies exceeds the rate of production of locally mixed fluid by interfacial instabilities. In general, for $Ri_B < 5$ the entrainment is turbulent-transport limited, for $Ri_B > 5$ it is interfacial-mixing limited, and at $Ri_B \sim 5$ both the transport and mixing rates are comparable yielding the maximum mixing efficiency $Ri_f \simeq 0.4$. For $3 < Ri_B < 5$, the intermediate-layer buoyancy frequency N_I is of the same order as the forcing frequency of the adjacent turbulent eddies w_{rms}/δ_{bh}, ensuring effective energy transfer to the interfacial area. This, together with mutually resonating K-H and asymmetric waves, appears to be responsible for the higher entrainment (interfacial erosion) rates observed for the two-layer case and largest disparity of entrainment rates observed between two-layer and linearly stratified cases for $3 < Ri_B < 5$.

Stratified turbulent shear flow research within the Environmental Fluid Dynamics Laboratory at Arizona State University is sponsored by the Office of Naval Research (Physical Oceanography Program), Army Research Office (Geosciences Division) and the National Science Foundation. The authors wish to gratefully acknowledge this support. Furthermore, we wish to thank Drs C. Y. Ching and I. P. D. DeSilva, Professors J. C. R. Hunt and E. Kit and Mr Leonard Montenegro for their endless support. Experimental assistance was provided by Mr Brian P. Martin, who was supported by an ONR high school traineeship award. We also wish to express our gratitude to the three referees whose comments led to substantial improvements to this paper.

REFERENCES

Abarbanel, H. D. I., Holm, D. D., Marsden, J. E. & Ratiu, T. 1986 Effect of variation in density on the stability of superposed streams. *Phil. Trans. R. Soc. Lond.* **318**, 349.

André, J. C. & Lacarrère, P. 1986 Mean and turbulent structure of the oceanic surface layer as determined from one-dimensional third order simulations. *J. Phys. Oceanogr.* **15**, 121–132.

Charnock, H. 1955 Wind-stress on a water surface. *Q. J. R. Met. Soc.* **81**, 639–640.

Christodoulou, G. C. 1986 Interfacial mixing in stratified flows. *J. Hydraul. Res.* **24**, 77–92.

Csanady, G. T. 1978 Turbulent interface layers. *J. Geophys. Res.* **83**(C5), 2329–2342.

Deardorff, J. W. & Willis, G. E. 1982 Dependence of mixed-layer entrainment on shear stress and velocity jump. *J. Fluid Mech.* **115**, 123–149.

DeSaubies, Y. & Smith, W. K. 1982 Statistics of Richardson number and instability in oceanic internal waves. *J. Phys. Oceanogr.* **12**, 1245–1259.

De Silva, I. P. D. 1991 Studies of turbulent mixing in stratified turbulent patches. PhD thesis, Arizona State University.

De Silva, I. P. D., Brandt, A., Montenegro, L. & Fernando, H. J. S. 1999 Gradient Richardson number measurements in a stratified shear layer. *Dyn. Atmos. Oceans* **30**, 47–63.

De Silva, I. P. D., Fernando, H. J. S., Eaton, F. & Hebert, D. 1996 Evolution of Kelvin–Helmholtz billows in nature and laboratory. *Earth Planet. Sci. Lett.* **143**, 217–231.

De Silva, I. P. D., Montenegro, L. & Fernando, H. J. S. 1990 Measurement of interfacial distortions at a stratified entrainment interface. *Expts. in Fluids* **9**, 174–177.

Dillon, T. M., Moum, J. N., Chereskin, T. K. & Caldwell, D. R. 1989 Zonal momentum balance at the equator. *J. Phys. Oceanogr.* **19**, 561–570.

E, X. & Hopfinger, E. J. 1986 On mixing across an interface in stably stratified fluid. *J. Fluid Mech.* **166**, 227–244.

Ellison, T. H. & Turner, J. S. 1959 Turbulent entrainment in stratified flows. *J. Fluid Mech.* **6**, 423–448.

ERIKSEN, C. C. 1978 Measurements and models of fine structure, internal gravity waves and breaking in the deep ocean. *J. Geophys. Res.* **83**(C6), 2989–3009.

FERNANDO, H. J. S. 1986 On buoyancy transfer across an entrainment interface. *Boundary-layer Met.* **34**, 171–176.

FERNANDO, H. J. S. 1991 Turbulent mixing in stratified fluids. *Ann. Rev. Fluid Mech.* **23**, 455–493.

FERNANDO, H. J. S. & HUNT, J. C. R. 1996 Some aspects of turbulence and mixing in stably stratified layers. *Dyn. Atmos. Oceans* **23**, 35–62.

FERNANDO, H. J. S. & HUNT, J. C. R. 1997 Turbulence, waves and mixing at shear-free density interfaces. Part 1. A theoretical model. *J. Fluid Mech.* **347**, 197–234.

FRITTS, D. C., ARENDT, S. & ANDREASSEN, O. 1998 Vorticity dynamics in a breaking internal gravity wave. Part 1. Initial instability evolution. *J. Fluid Mech.* **367**, 27–46.

GARGETT, A. E., OSBORN, T. R. & NASMYTH, P. W. 1984 Local isotropy and the decay of turbulence in a stratified fluid. *J. Fluid Mech.* **144**, 231–280.

GARRETT, C. & MUNK, W. 1972 Oceanic mixing by breaking internal waves. *Deep-Sea Res.* **19**, 823–832.

GARTSHORE, I. S., DURBIN, P. A. & HUNT, J. C. R. 1983 The production of turbulent stress in a shear flow by irrotational fluctuations. *J. Fluid Mech.* **137**, 307–329.

GOLDSTEIN, S. 1931 On the stability of superposed streams of fluids of different densities. *Proc. R. Soc. Lond.* A **132**, 524–548.

HAIGH, S. P. & LAWRENCE, G. A. 1999 Symmetric and non-symmetric Hölmböe instabilities in an inviscid flow. *Phys. Fluids* **11**, 1459–1468.

HANNOUN, I. A. & LIST, E. J. 1988 Turbulent mixing at a shear free density interface. *J. Fluid Mech.* **189**, 211–234.

HAZEL, P. 1972 Numerical studies of the stability of inviscid stratified shear flows. *J. Fluid Mech.* **51**, 39–61.

HÖLMBÖE, J. 1962 On the behavior of symmetric waves in stratified shear layers. *Geophys. Publ.* **24**, 67–72.

HOWARD, L. N. 1961 Note on a paper of John W. Miles. *J. Fluid Mech.* **10**, 509–512.

HUPPERT, H. E., TURNER, J. S. & HALLWORTH, M. A. 1995 Sedimentation and entrainment in dense layers of suspended particles stirred by an oscillating grid. *J. Fluid Mech.* **289**, 263–293.

KANTHA, L. H. 1977 Note on the role of internal waves in thermocline erosion. In *Modelling and Prediction of the Upper Layers of the Ocean* (ed. E. B. Kraus), pp. 173–177. Pergamon.

KANTHA, L. H., PHILLIPS, O. M. & AZAD, R. S. 1977 On turbulent entrainment at a stable density interface. *J. Fluid Mech.* **79**, 753–768.

KATO, H. & PHILLIPS, O. M. 1969 On the penetration of a turbulent layer into stratified fluid. *J. Fluid Mech.* **37**, 643–655.

KIT, E., STRANG, E. J. & FERNANDO, H. J. S. 1997 Measurement of turbulence near shear-free density interfaces. *J. Fluid Mech.* **334**, 293–314.

KLAASSEN, G. P. & PELTIER, W. R. 1989 The role of transverse secondary instabilities in the evolution of free shear layers. *J. Fluid Mech.* **202**, 367–402.

KOOP, C. G. & BROWAND, F. K. 1979 Instability and turbulence in a stratified fluid with shear. *J. Fluid Mech.* **93**, 135–159.

KUNDU, P. K. & BEARDSLEY, R. C. 1991 Evidence of a critical Richardson number in moored measurements during the upwelling season off Northern California. *J. Geophys. Res.* **37**, 643–655.

LAWRENCE, G. A., BROWAND, F. K. & REDEKOPP, L. G. 1991 The stability of a sheared density interface. *Phys. Fluids* A **3**, 2360–2370.

LINDEN, P. F. 1975 The deepening of a mixed layer in a stratified fluid. *J. Fluid Mech.* **71**, 385–405.

LOFQUIST, K. 1960 Flow and stress near an interface between stratified liquids. *Phys. Fluids* **3**, 158–175.

MAHRT, L. & LENSCHOW, D. H. 1976 Growth dynamics of the convectively mixed layer. *J. Atmos. Sci.* **33**, 41–51.

MANINS, P. C. & SAWFORD, B. L. 1979 A model of katabatic winds. *J. Atmos. Sci.* **36**, 619–630.

MILES, J. W. 1961 On the stability of heterogeneous shear flows. *J. Fluid Mech.* **10**, 496–508.

MILES, J. W. 1986 Richardson's criterion for the stability of stratified shear flow. *Phys. Fluids* **29**, 3470–3471.

Moum, J. N., Caldwell, D. R. & Paulson, C. A. 1989 Mixing in the equatorial surface layer. *J. Geophys. Res.* **94**, 2005–2021.

Narimousa, S. & Fernando, H. J. S. 1987 On the sheared density interface of an entraining stratified fluid. *J. Fluid Mech.* **174**, 1–22.

Narimousa, S., Long, R. R. & Kitaigorodskii, S. A. 1986 Entrainment due to turbulent shear flow at the interface of a stably stratified fluid. *Tellus* **38**A, 76.

Noh, Y. & Fernando, H. J. S. 1991 Dispersion of suspended particles in turbulent flow. *Phys. Fluids* A **3**, 1730–1740.

Odell, G. M. & Kovasznay, L. S. G. 1971 A new type of water channel with density stratification. *J. Fluid Mech.* **50**, 535–543.

Orlanski, I. & Bryan, K. 1969 Formation of the thermocline step structure by large-amplitude internal gravity waves. *J. Geophys. Res.* **50**, 535–543.

Papantoniou, D. & List, E. J. 1989 Large-scale structure in the far field of buoyant jets. *J. Fluid Mech.* **209**, 151–190.

Pardyjak, E., Fernando, H. J. S., Anderson, J. & Berman, N. S. 1999 Breakdown of complex terrain atmospheric boundary layers. *Bull. Am. Phys. Soc.* **44**, 171.

Perera, M. J. A. M., Fernando, H. J. S. & Boyer, D. L. 1994 Turbulent mixing at an inversion layer. *J. Fluid Mech.* **267**, 275–298.

Pollard, R. T., Rhines, P. B. & Thompson, R. O. R. Y. 1973 The deepening of the wind-mixed layer. In *Geophysical Fluid Dynamics*, pp. 381–404. Gordon and Breach.

Price, J. F., Weller, R. A. & Pinkel, R. 1986 Diurnal cycle: Observations and models of the upper ocean response to diurnal heating, cooling and wind mixing. *J. Geophys. Res.* **91**, 8411–8427.

Richardson, L. F. 1920 The supply of energy from and to atmospheric eddies. *Proc. R. Soc. Lond.* A **97**, 354–373.

Spigel, R. H., Imberger, J. & Rayner, K. N. 1986 Modeling the diurnal mixed layer. *Limnol. Oceanogr.* **31**, 533–556.

Staquet, C. 1995 Two-dimensional secondary instabilities in a strongly stratified shear layer. *J. Fluid Mech.* **296**, 73–126.

Stephenson, P. W. & Fernando, H. J. S. 1991 Turbulence and mixing in a stratified shear flow. *Geophys. Astrophys. Fluid Dyn.* **59**, 147–164.

Strang, E. J. 1997 Entrainment and mixing in stratified shear flows. PhD thesis, Arizona State University.

Strang, E. J. & Fernando, H. J. S. 2000 Vertical mixing and transports through a stratified shear layer. *J. Phys. Oceanogr.*, In press.

Sullivan, G. D. & List, E. J. 1993 An experimental investigation of vertical mixing in two-layer density-stratified shear flows. *Dyn. Atmos. Oceans* **19**, 147–174.

Sullivan, G. D. & List, E. J. 1994 On mixing and transport at a sheared density interface. *J. Fluid Mech.* **273**, 213–239.

Taylor, G. I. 1931 Effect of variation in density on the stability of superposed streams. *Proc. R. Soc. Lond.* A **132**, 499–523.

Thompson, R. O. R. Y. 1984 Formation of thermoclines in zero-mean-shear turbulence. *J. Geophys. Res.* **89**, 8017–8021.

Thorpe, S. A. 1968 A method of producing a shear flow in a stratified fluid. *J. Fluid Mech.* **32**, 693–704.

Thorpe, S. A. 1973 Experiments on instability and turbulence in a stratified shear flow. *J. Fluid Mech.* **61**, 731–751.

Thorpe, S. A. 1977 Turbulence and mixing in a Scottish Loch. *Phil. Trans. R. Soc. Lond.* A **286**, 125–181.

Townsend, A. A. 1966 Internal waves produced by a convective layer. *J. Fluid Mech.* **24**, 307–319.

Turner, J. S. 1973 *Buoyancy Effects in Fluids*. Cambridge University Press.

Turner, J. S. 1986 Turbulent entrainment: the development of the entrainment assumption, and its application to geophysical flows. *J. Fluid Mech.* **173**, 431–471.

Wijesekera, H. W. & Dillon, T. M. 1991 Internal waves and mixing in the upper equatorial Pacific ocean. *J. Geophys. Res.* **96**, 7115–7125.

Zic, K. & Imberger, J. 2000 Energy leakage from a surface mixing layer. *Submitted for publication.*